# Loss of Sarm1 non-autonomously protects Schwann cells from chemotoxicity

**Weili Tian*, Tim Czopka§ and Hernán López-Schier***

* Sensory Biology & Organogenesis, Helmholtz Zentrum Munich, Germany

§ Institute of Neuronal Cell Biology, Technical University of Munich, Germany

**Correspondence to**: hernan.lopez-schier@helmholtz-muenchen.de

**Abbreviated title:** Sarm1 and glioprotection

**Keywords**: Wallerian degeneration, Sarm1, Schwann cells, regeneration

**Acknowledgements**: This research was supported by a Grant from the Human Frontiers Science Programme and by the Helmholtz Gemeinschaft to H.L-S.

**ABSTRACT**

The obligate pro-degenerative protein Sarm1 is essential for Wallerian axon degeneration. Inhibition of Sarm1 has been proposed as a promising neuroprotective strategy with clinical relevance. Yet, the conditions that will most benefit from inhibiting Sarm1 remain undefined. Here we use genetics and pharmacology in zebrafish to show that systemic elimination of Sarm1 is glioprotective. Loss of Sarm1 does not affect macrophage recruitment to the wound microenvironment, focal injury resolution, or nerve repair. Unexpectedly, Sarm1 deficiency increases Schwann-cell resistance to toxicity by diverse chemotherapeutic agents after neuronal injury. Yet, synthetic degradation of Sarm1-deficient severed axons reversed this effect, suggesting that glioprotection is non-cell-autonomous. These findings anticipate that interventions aimed at inhibiting Sarm1 can counter heightened glial vulnerability to chemical stressors and may be an effective strategy to reduce chronic consequences of neurotrauma.

## INTRODUCTION

The peripheral nerves that communicate skin, muscle and sensory organs with the brain must maintain functionality throughout life despite frequent stress and trauma (1-6). Loss of integrity of peripheral neurons and associated cells, including glia, is a common occurrence in severe neurological dysfunctions that include weakness, pain and loss of sensation (7). Glial loss leads to nerve demyelination, defasciculation and neuronal death. Nerve injury triggers axon fragmentation and degeneration. In turn, this induces the dedifferentiation of associated glial cells, which enhances glial role in nerve repair. However, dedifferentiation also makes glia vulnerable to degeneration after protracted denervation (8-12). Damaged axons undergo Wallerian degeneration (13), which is regulated by the evolutionary ancient pro-degenerative protein Sarm1 (Sterile Alpha and TIR Motif containing 1) (14-17). Sarm1 is a modular protein that contains two sterile-alpha motifs (SAM), one mitochondrial association (MT) and one TIR domain (14). Nerve injury activates Sarm1 by TIR dimerization, which is sufficient to induce the axon degeneration (18, 19). Mechanistically, Sarm1 activation results in the loss of nicotinamide adenine dinucleotide (NAD+) in damaged axons (20-22). The TIR domain acts as a NADase (23), explaining why over-expression of the NAD+ synthesizing enzyme NMNAT1 inhibits the degradation of severed axons by sustaining high levels of NAD+ downstream of Sarm1 (24). Moreover, the loss of Sarm1 blocks the degeneration of injured axons, and forced activation of Sarm1 induces axon destruction in the absence of injury. Therefore, Sarm1 is a cell-autonomous hierarchical regulator of a signaling pathway that is necessary and sufficient for axonal degradation (22). Upon

23 peripheral-nerve injury, glial Schwann cells acquire a specialized function that
24 promotes the clearance of axon fragments ahead of axonal re-growth from the
25 proximal stump that remains associated to the neuronal perikaryon (25). Expeditious
26 axonal regeneration is important because sustained Schwann-cell denervation leads
27 to protracted loss of glial terminal phenotype and eventual death. In turn, glial loss
28 impairs regenerating nerve myelination and circuit repair, transforming acute
29 neuropathies into irreversible chronic neurological dysfunction. Therefore, inhibiting
30 or delaying axon destruction has been hypothesized as an effective strategy to counter
31 heightened Schwann-cell vulnerability to additional stressors that include metabolic
32 imbalance and drugs (26, 27). This idea has sparked intense efforts to identify specific
33 molecular inhibitors of axon degeneration for clinical applications (28, 29). As a
34 discrete hierarchical factor that is essential for axon degeneration, Sarm1 is an ideal
35 target for pharmacological interventions (18). However, the conditions that would
36 most benefit from inhibiting Sarm1 systemically are yet to be defined (30, 31).
37
38 Here we address the above issue using the powerful genetics of zebrafish, a small
39 vertebrate whose nervous system is anatomically simpler but structurally and
40 functionally similar to that of mammals (32-34). Crucially, the zebrafish larva is ideal
41 to study Schwann-cell biology in the natural context of the behaving animal (35-42).
42 By characterizing loss-of-function mutations in Sarm1, we provide novel insights into
43 the cellular basis of axon-glia interactions, and provide data that encourage the quest
44 to identify and develop Sarm1 inhibitors for clinical applications.
45

46 **RESULTS**

47 **Identification and mutagenesis of Sarm1 in zebrafish**

48 The amino-acid sequence of Sarm1 is well conserved across species (15, 43). To
49 identify Sarm1 orthologs in zebrafish, we scanned publicly accessible genomic data
50 (*Danio rerio* reference genome assembly version GRCz11) by a BLAST search using
51 the TIR domain, which is present in all known Sarm1 proteins (15, 44). This
52 exploration yielded a single candidate *locus* in chromosome 15. No other part of the
53 zebrafish genome appears to harbor Sarm1 paralogs. The genomic structure of the
54 putative zebrafish Sarm1 reminisces that of other species, containing 8 exons that
55 code for a protein of 713 amino acids, with the typical N-terminal auto-inhibitory
56 domain, two central SAM multimerization domains and a C-terminal TIR
57 degeneration domain (Figure 1A). Similar to *D. melanogaster*, however, *D. rerio* Sarm1
58 lacks an obvious mitochondria-targeting sequence (MT). To test whether the
59 identified gene produces a protein with the expected functional role, we used
60 CRISPR/Cas9-mediated genome modification to generate loss-of-function
61 mutations in Sarm1. By targeting exon 1, we obtained germ-line transmission of two
62 alleles: $sarm1^{hzm13}$ and $sarm1^{hzm14}$ (Supplemental Figure 1A-B). The hzm13 allele
63 introduces an 11-base deletion and T/C mutation, resulting in a frame shift and
64 premature stop codon. hzm14 is a 7-base deletion and AG/GA mutation that also
65 generates a frame shift and premature stop codon. Analysis of protein extracts from
66 wild-type embryos by Western-blot using an antibody to Sarm1 revealed a single
67 band of approximately 80kDa, which agrees with the expected size of the full-length
68 protein (Supplemental Figure 1C). This band was absent in protein extracts from

69 homozygous *sarm1*$^{hzm13}$ zebrafish embryos. Of note, because this antibody recognizes
70 an epitope in the C-terminus of Sarm1, it does not allow to discriminate between the
71 expression of a truncated protein lacking all the domains with known function, and
72 the complete absence of Sarm1 induced by nonsense-mediated mRNA decay.
73 Homozygous *sarm1*$^{hzm13}$ mutants display no overt anatomical defects (Supplemental
74 Figure 1D-E), are viable and develop into fertile adults (not shown). Furthermore, a
75 simple assay for sensorimotor function that consists of eliciting the escape response
76 after tactile stimuli showed that the displacement distance and the average
77 acceleration were no different between wild type and Sarm1 mutants (Supplemental
78 Figure 1F-G) (45).
79
80 **Functional conservation of Sarm1 in Wallerian axon degeneration**
81 Although Sarm1 has already been extensively studied in neurons of *Drosophila* and
82 mammals, we wanted to assess the effects of systemic loss of Sarm1 on neuronal and
83 non-neuronal cells in larval zebrafish. The reason is that no single study has
84 addressed Sarm1 function holistically, in a single organism, by *in toto* live microscopic
85 imaging. To this end, we used several parameters of nervous-system structure and
86 function by combining *sarm1*$^{hzm13}$ with various transgenes expressing fluorescent
87 markers in the sensory neurons of the mechanosensory lateral line, as well as in their
88 associated Schwann cells (46, 47). The lateral-line system is ideal for *in vivo* studies at
89 high resolution over extended periods, and for physiological studies under normal
90 and altered conditions (48-51). It combines the organization of a typical vertebrate
91 sensory system with the amenability for controlled experimental interventions that

92 include microsurgery, pharmacology and optogenetics (41, 42, 52, 53). We found
93 that loss of Sarm1 does not affect the development and maintenance of the lateral-
94 line sensory pathway (Supplemental Figure 1H-N). Next, we assessed neuronal
95 intracellular dynamics and physiological function. To this end, we fluorescently
96 marked mitochondria in lateralis neurons by expressing the mitochondria targeting
97 sequence of the Cytochrome-C oxidase subunit 8A fused to mCherry (54). We chose
98 mitochondria because mitochondria produce energy for the neurons and also
99 regulate calcium levels, which are critical for the function and viability of axons and
100 neurons. These intracellular organelles are dynamic and distribute throughout the
101 neuron by active transport mediated by molecular motors that move along
102 microtubule tracks. In axons, microtubules are polarized such that their plus ends are
103 directed toward the axon terminals, in turn orienting the movement of distinct
104 molecular motors in the antero- and retro-grade directions (55). Intra-axonal
105 movement direction also reflects mitochondrial fitness because stressed organelles are
106 biased in the retrograde direction (56, 57). Therefore, axonal mitochondria represent
107 an optimal proxy for neuronal polarization, intracellular dynamics and overall
108 cellular health. We found a qualitatively similar number, density and distribution of
109 mitochondria in the peripheral axons of wild type and Sarm1 mutants. Kymographic
110 analysis revealed a majority of static large mitochondrial groups, and some smaller
111 fragments moving persistently substantial distances at constant velocity in the
112 anterograde and retrograde directions (Figure 1B-C). Importantly, quantifications
113 showed no significant differences in the number and spatial distribution of axonal

114 mitochondria (Figure 1D), or movement velocity and direction between wild-type
115 and mutant animals (Figure 1E).
116
117 Next, we assayed functional conservation of Sarm1 in this neuronal pathway using a
118 previously established bioassay of neurotrauma, which employs intact larval zebrafish,
119 laser-mediated severing individualized axons by single-neuron fluorescent-protein
120 expression, and high-resolution intravital microscopy (41,58). Axotomy was done by
121 focusing an ultraviolet laser beam to a discrete region of peripheral nerve. Upon
122 severing, the distal axon segment quickly degenerates in wild-type specimens,
123 whereas the proximal segment that remains associated with the neuronal perikaryon
124 remains viable (Figure 1F). Kinetic analysis shows that severed Sarm1-deficient axon
125 segments resisted degeneration for over 5 days. The degeneration-resistant
126 phenotype was rescued by the transgenic introduction of a fluorescent-tagged full-
127 length Sarm1 in mutant neurons (Figure 1G).
128
129 **Loss of Sarm1 does not affect focal damage resolution**
130 Physical injury often results in inflammatory responses that recruit immune cells to
131 the wound. After nerve injury, Schwann cells release chemoattractants for
132 macrophages before axon fragmentation is evident. Injury-mediated production of
133 reactive oxygen species (ROS) recruits inflammatory cells, including macrophages.
134 Studies *ex vivo* using mammalian cultured neurons showed that Sarm1 acts
135 downstream of mitochondrial ROS generation. Therefore, we decided to test *in vivo*
136 if the loss of Sarm1 as well as the absence of Schwann cells would affect macrophage

137 recruitment to the site of injury. To this end, we generated a transgenic line
138 expressing membrane-targeted EGFP under the control of the macrophage-specific
139 promoter Mfap4. We combined this line with Tg[SILL:mCherry] and mutations in
140 Sarm1 or Erbb2. Loss of Erbb2 in zebrafish impairs Schwann-cell migration along
141 lateral-line axons and leads to nerve unmyelination and defasciculation (53, 59). We
142 first injured nerves with the laser and assessed macrophage behavior at high
143 resolution. We found that the onset of recruitment and number of macrophages at
144 the wound did not differ between wild-type specimens and Sarm1 or Erbb2 mutants
145 (Figure 2A and Supplemental Movies 1-3). Macrophages arrived from various
146 locations moved along the proximal and distal part of the axons in wild-type and
147 mutant specimens. The retention time of macrophages at the proximal side of the
148 wound was unaltered in Sarm1 or Erbb2 mutants, although on average slightly
149 lengthened in the absence of Schwann cells (Figure 2B). In wild type, and Sarm1 and
150 Erbb2 mutants, macrophages engulfed debris locally at the injury site, and did not
151 appear to be involved in the degradation of the distal part of the severed axons
152 (Supplemental Movies 1-3). We found, however, a significant increase in the size of
153 the engulfed debris by macrophages in Erbb2-mutant animals (Figure 2C). These
154 results reveal that the loss of Sarm1 does not affect focal damage resolution by
155 macrophages, which are recruited to the wound independently of Schwann cells. We
156 did notice discrete and highly mobile axon fragments that were not associated to
157 EGFP(+) cells in wild-type and Erbb2-mutant animals, but not in Sarm1-deficient
158 fish. This observation suggests that activated phagocytic cells other than

159 macrophages and Schwann cells engulf and clear distal axon fragments after damage,
160 and that this does not occur in Sarm1-/- animals.
161
162 **Synthetic elevation of axoplasmic $Ca^{2+}$ induce degradation of severed**
163 **Sarm1-deficient axons**
164 Calcium ($Ca^{2+}$) regulation in neurons is critical for homeostasis because sustained
165 elevation of cytosolic calcium leads to axonal and neuronal degeneration. Often, this
166 occurs because mitochondria release apoptosis-inducing factors and proteases in a
167 calcium-dependent manner (60). Studies of mammalian neurons *in vitro* and of
168 zebrafish have shown that neuronal damage triggers two waves of elevation of
169 axoplasmic calcium ($Ca^{2+}$) (21, 52). The first occurs nearly immediately after injury
170 and decays rapidly, whereas the second has slower onset and decay. Loss of Sarm1
171 prevents $Ca^{2+}$ elevation in severed axons (21). We sought to further test the functional
172 conservation of Sarm1 in zebrafish *in vivo* by monitoring $Ca^{2+}$ dynamics in lateralis
173 sensory axons at high-resolution before and after injury. We measured $Ca^{2+}$
174 dynamics *in toto* at high-resolution before and after axon injury using the genetically-
175 encoded sensor GCaMP7a, to find that intact wild-type and Sarm1-mutant axons
176 show undetectable levels of axoplasmic fluorescence above background (Figure 3A).
177 Upon severing, fluorescent signal in wild-type axons distal segments increased
178 immediately and subsequently decayed with a near constant slope, whereas
179 fluorescence remained nearly undetectable in Sarm1-deficient distal axon segments
180 (Figure 3B). Next, we examined the $Ca^{2+}$ levels in mitochondria and the endoplasmic
181 reticulum (ER) using genetically encoded vital sensors, respectively Mito-RGECO

182 and ER-GCaMP3 (Figure 3C-F). We selected these organelles because $Ca^{2+}$ release
183 from the axonal ER activates the mitochondrial permeability transition pore to
184 trigger axonal degeneration (61, 62). We found that both mitochondrial and reticular
185 $Ca^{2+}$ levels increased equally after axon severing in severed wild-type and Sarm1-/-
186 axons. These results reveal that loss of Sarm1 attenuates calcium influx to the
187 axoplasm, but not $Ca^{2+}$ uptake in mitochondria or the ER.
188
189 Because the second $Ca^{2+}$ wave is responsible for the activation of the serine-threonine
190 protease Calpain, which in turn facilitates axonal fragmentation by cleaving
191 microtubules and neurofilaments (63), we decided to monitor $Ca^{2+}$ levels in lateralis
192 sensory axons 2, 4, 8 and 12 hours-post-injury (hpi). In severed wild-type axons, the
193 second wave of axoplasmic $Ca^{2+}$ starts 4 hpi in coincidence with axon fragmentation,
194 and remains elevated in axonal debris up until 8 hpi (Figure 3G). Note that the
195 temporal resolution of these images does not allow the resolution of degeneration
196 before axonal regeneration. By contrast, the second wave of axoplasmic $Ca^{2+}$ does
197 not occur in Sarm1-mutant axons (Figure 3H). Thus, we hypothesized that forcing a
198 sustained elevation of axoplasmic $Ca^{2+}$ will be sufficient to trigger the degradation of
199 severed Sarm1-deficient axons. To test this prediction, we transgenically expressed
200 the rat transient receptor potential cation channel subfamily V member 1 (TRPV1)
201 fused to tagRFP in lateralis afferent neurons of Sarm1-mutant zebrafish. Expression
202 of mCherry alone in neurons served as control. TRPV1 is non-selective cation
203 channel that exhibits a high divalent selectivity, and whose activation produces an
204 influx of $Ca^{2+}$ into cells (64). Rat TRPV1 is activated by temperatures above 43°C

205 or by the vanilloid capsaicin. Importantly, this TRPV1 is inactive at the temperature
206 used to maintain zebrafish (28°C), and zebrafish TRPV1 orthologs are insensitive to
207 capsaicin (65). Therefore, rat TRPV1 expressed in zebrafish offers a tunable tool to
208 elevate axoplasmic $Ca^{2+}$ with excellent temporal resolution. We severed TRPV1-
209 expressing and mCherry-expressing lateralis axons, and 2 hours later a vehicle
210 solution or vehicle + capsaicin were added in the water holding the fish
211 (Supplemental Figure 2A-B). Samples were inspected 90 minutes later. Severed
212 Sarm1-deficient axons not expressing TRPV1 did not fragment in presence of
213 capsaicin, or TRPV1-expressing axons bathed in ethanol solution. As hypothesized,
214 we found that Sarm1-deficient TRPV1-expressing axon segments readily degraded
215 in the presence of capsaicin (Supplemental Figure 2C-F). Thus, elevation of
216 axoplasmic $Ca^{2+}$ downstream of Sarm1 is sufficient to trigger axon degradation *in vivo*.
217

218 **Schwann cells are not essential to maintain Sarm1-/- axon segments**

219 The Schwann cells support, fasciculate and myelinate sensory axons in vertebrates
220 (66). We reasoned that delayed axon degeneration by loss of Sarm1 might impact the
221 interaction between axons and Schwann cells. To assess this interaction *in vivo*, we
222 combined the *sarm1*$^{hzm13}$ allele with the triple transgenic line *Tg[gSAGFF202A ; UAS-*
223 *GFP ; SILL:mCherry]* to highlight the Schwann cells with green fluorescence and the
224 lateralis afferent neurons with red fluorescence (53, 67). Using high-resolution
225 intravital microscopy, we ascertained that Schwann cells develop normally and
226 fasciculate sensory axons in Sarm1-deficient zebrafish (Figure 4A). Upon severing,
227 wild-type axons were quickly cleared by the Schwann cells through engulfment of

228 axonal fragments and intracellular degradation of debris (Figure 4B). However, there
229 was no axon fragmentation or phagocytic activity by the Schwann cells in Sarm1
230 mutants (Figure 4C). Next, we asked if Schwann cells are necessary for the
231 maintenance of severed Sarm1-deficient axons by generating a double mutant
232 zebrafish line concurrently deficient for Erbb2 and Sarm1. In Erbb2-deficient
233 specimens, the distal portion of the severed axons fragmented and were cleared
234 (Figure 4C) but with a significant delay compared to wild-type specimens (Figure 4D).
235 By contrast, in Erbb2/Sarm1 double mutants, severed axons did not fragment or
236 degrade, identically to fish lacking only Sarm1 (Figure 4D). Thus, axon maintenance
237 in Sarm1 mutants occurs independently of the Schwann cells, and that their eventual
238 clearance is performed by other cells.
239
240 When an injury generates a gap in the glia, wound-adjacent Schwann cells actively
241 move and extend cellular projections resembling filopodia to quickly reconstitute a
242 continuous glial scaffold (53). Although continuous glia are not necessary for the re-
243 growth of the proximal axon stump, it prevents regenerating growth cones from
244 straying, in turn facilitating end-organ *de novo* innervation and circuit reconstitution
245 (39, 41). Thus, we decided to interrogate Schwann-cell behavior immediately after
246 axon severing and during axon regeneration combining *Tg[gSAGFF202A;UAS-GFP ;*
247 *SILL:mCherry]* double transgene with the Sarm1 mutation. As expected, we found that
248 in wild-type animals, the Schwann cells adjacent to the wound quickly extended
249 filopodia to close the gap in the glial scaffold ahead of axonal regeneration
250 (Supplemental Movie 4). Re-growing fibers then followed these sub-cellular glial

251 bridges to reconstitute the nerve, suffering mild defasciculation restricted to a small
252 area within the injury (Figure 4E and Supplemental Figure 3). In stark contrast,
253 injury-adjacent Schwann cells did not migrate or produce filopodia-like projections
254 in Sarm1 mutants (Supplemental Movie 5). Nonetheless, regenerating axons
255 eventually negotiated the persistent larger gap to grow along the distal glial scaffold.
256 However, the reforming nerves presented more pronounced local defasciculation
257 (Figure 4F and Supplemental Figure 4).
258

259 **Loss of Sarm1 does not alter Schwann-cell phenotype after axotomy**

260 Denervated Schwann cells undergo partial dedifferentiation from myelinating to a
261 progenitor-like state as revealed by loss of expression of terminal-phenotype markers,
262 including myelin and myelin-associated proteins (25, 68, 69). The loss of terminal
263 phenotype promotes Schwann-cell proliferation and migration, which enhances their
264 regenerative function (70). We hypothesized that because Schwann-cell denervation
265 does not occur in Sarm1-mutants, distal Schwann cells may not dedifferentiate. This
266 would explain their lack of phagocytic and protrusive activities after axon transection.
267 Following this rationale, we immunostained samples with an antibody to Claudin-k,
268 which localizes to the junctions between mature Schwann cells and is downregulated
269 in denervated glia (41, 71). In wild-type specimens, Claudin-k remained strongly
270 expressed along the entire length of the lateralis afferent nerve up to 6 hours after
271 nerve injury (hpi), suggesting that distal Schwann cells remain mature during distal-
272 axon fragmentation (Figure 5A-B). Beginning at 10 hpi, however, distal Schwann
273 cells had markedly less Claudin-k than proximal cells. Finally, 24 hpi Claudin-k was

274 conspicuously absent from distal Schwann cells even after axons regeneration had
275 commenced. By contrast, Claudin-k remained strongly expressed after axon severing
276 in Sarm1-mutant animals during the same period, with no apparent difference
277 between Schwann cells located at either side of the wound (Figure 5A,C).
278
279 Next, we assessed myelination using the 6D2 monoclonal antibody, which recognizes
280 a carbohydrate epitope in the piscine P0-like myelin glycoproteins IP1 and IP2 (72,
281 73). As with Claudin-k, 6D2 labeling faded in Schwann cells distal to the injury in
282 wild-type specimens (Figure 6A). Yet, 6D2 labeling remained unchanged in Sarm1
283 mutants (Figure 6B). We obtained congruent results when addressing myelination
284 directly in living specimens by using a transgenic line expressing membrane-targeted
285 EGFP under the control of the myelin binding protein (Mbp:EGFP-CAAX, green)
286 (Figure 6C-D) (74). Together, these results indicate that Sarm1-deficient sensory
287 axons are maintained independently of Schwann-cell support, and that the clearance
288 the severed axons is not necessary for regenerating axon growth, pathfinding,
289 myelination and re-innervation of sensory organs. In addition, they reveal that
290 Schwann cells distal to the injury do not de-differentiate in Sarm1-mutant specimens.
291
292 **Loss of Sarm1 counteracts Schwann-cell vulnerability to chemical toxins**
293 Many chemotherapeutic agents invariably cause peripheral neurotoxicity, leading to
294 permanent neuronal dysfunction (75-79). Under conditions of denervation, Schwann
295 cells become strongly susceptible to chemotoxicity (80). We wondered if the
296 protracted maintenance of severed axons in Sarm1 mutants may suppress glial

297 vulnerability. To test this idea, we treated wild-type and Sarm1-mutant zebrafish
298 with several chemical compounds that are under clinical trials or used as first-line
299 treatment for common cancers in humans. First, we used 10-Hydroxycamptothecin
300 (10-HCT), which is extremely toxic to denervated glia (82), and counted Schwann
301 cells using the fluorescence transgenic marker *Tg[gSAGFF202A ; UAS:EGFP]*, which
302 is ideal for this experiment because the intensity of green fluorescence does not vary
303 in denervated Schwann cells and, therefore, is independent of the maturity of these
304 glia (41). We confirmed that 10-HCT does not affects in Schwann cells associated to
305 viable axon (Figure 7A-B). However, it significantly reduced the number of Schwann
306 cells in 10-HTC-treated wild-type animals after axon severing. By contrast, the
307 number of distal Schwann cells was only marginally affected in Sarm1-mutant
308 specimens (Figure 7B). Platinum-based, taxanes and some alkaloids are effective
309 chemotherapeutic agents used as standards-of-care for various human malignancies,
310 despite their severe neuropathic effects that include glial destruction (81). To address
311 their effect on Schwann cell, we treated wild-type or Sarm1 mutant zebrafish with
312 cisplatin, oxaliplatin, paclitaxel, docetaxel and vincristine. We found that upon nerve
313 transection, all these drugs invariably killed injury-distal Schwann cells in wild-type
314 specimens but not in Sarm1 mutants (Figure 7C). Importantly, none of these drugs
315 affected Schwann cells associated with intact axons, suggesting that axons protect
316 Schwann cells from chemical stress. To confirm this prediction, we forced the
317 degradation of severed axons in Sarm1-deficient zebrafish treated with 10-HCT or
318 vincristine. To this end, we repeated the used of capsaicin to activate rat TRPV1
319 expressed in a sub-set of lateralis neurons in homozygous mutant fish, in which

320 Sarm1 is absent from every cell, including Schwann cells. This experiment revealed
321 that Schwann cells lacking Sarm1 again become vulnerable to chemotoxicity once
322 severed axons were synthetically eliminated (Figure 7D), confirming that Sarm1-
323 mediated glioprotection is non-autonomous and depends upon the presence of non-
324 degradable axons.
325

326 **DISCUSSION**

327 The sensory neurons that innervate skin, sensory receptors, joints and muscle
328 communicate peripheral information to the brain, enabling animals to perform the
329 essential activities of daily life. Nerve loss has significant negative impact on the
330 quality of life of the affected individuals. Using zebrafish and a battery of tests that
331 include subcellular structural characterization of sensory neurons and associated
332 Schwann cells, neuronal-function, and behavioral assays, we offer a comprehensive
333 and integrated analysis of neuronal and glial response to injury, as well as on the
334 consequences of blocking axon degeneration systemically. It has been well established
335 that the absence of Sarm1 in *Drosophila* and the mouse prevents the degradation of
336 damaged axons (15, 83). Although we were not predicting any differences for Sarm1
337 in zebrafish, assaying functional conservation in our experimental neuronal pathway
338 is not dispensable because some neurotraumatic conditions had been shown to lead
339 to neuronal loss in the absence of Sarm1. Loss of Sarm1 improves functional recovery
340 after traumatic brain injury in mice, and inhibits vincristine-mediated neurotoxicity
341 (84, 85). Sarm1-deficient mice are viable (19, 86).We found that chronic and systemic
342 loss of Sarm1 is compatible with zebrafish viability and sensorineural function, and

343 demonstrate that the long-term maintenance of non-degradable axon fragments has
344 no detrimental effect on the repair of a sensory circuit. Furthermore, regenerating
345 axons fasciculate and myelinate normally, indicating that they do not compete with
346 non-degradable axons segments for exiting glia. Therefore, we conclude that the
347 axonal destructive and nerve reconstructive processes occur in parallel. In addition,
348 these data suggest that a competitive balance between axon degradation and
349 regeneration does not appear to have shaped the evolution of Sarm1 and, by
350 extension, Wallerian degeneration.
351
352 Focusing on Schwann cells, we show that glial cells adjacent to nerve injury in Sarm1
353 mutants behave dramatically different than those of wild-type specimens. Specifically,
354 Schwann cells in Sarm1 mutants do not migrate or extend projections to bridge the
355 gap in the glial scaffold, indicating that these cells do not directly sense missing
356 intercellular contacts or glial discontinuity. Instead, our findings suggest alternative
357 scenarios. One is that the degradation of axons releases signals that induce Schwann
358 cell to change behavior. In mice, for example, nerve damage promotes mesenchymal
359 behavior of Schwann cells surrounding the wound via TGF-β signaling, which drives
360 collective Schwann-cell migration across the wound (87). Although we did not
361 observe Schwann-cell migration, signals derived from injured axons may promote
362 wound-adjacent Schwann cells to extend projections to bridge the gap in a similar
363 manner. Interestingly, we observed that filopodia-like structures emerged from
364 Schwann cells at both sides of the injury in wild-type animals, suggesting that repair-
365 inducing signals are likely diffusible, affecting glial cells independently of their

366 association with axons. It remains to be determined if the source of such signals is the
367 damaged axons, the denervated Schwann cells, or other cells in the wound
368 microenvironment.
369
370 Upon nerve injury, activated macrophages rapidly accumulate around the wound
371 and contribute to Wallerian degeneration and to axonal regeneration. Specifically,
372 classical pro-inflammatory M1-type phagocytic macrophages remove axonal and
373 myelin debris, whereas anti-inflammatory M2-type macrophages modulate
374 Schwann-cell activity and promote axon regeneration. Immediately after nerve
375 injury, Schwann cells release chemokines that attract or retain macrophages at the
376 wound before axon fragmentation. Importantly, pharmacological activation of
377 macrophage recruitment to the wound microenvironment enhances axon
378 regeneration, whereas decrease of macrophage infiltration inhibits axon regeneration.
379 Reactive oxygen species (ROS) are conserved early wound signals across species.
380 Injury-mediated ROS production recruits inflammatory cells, including
381 macrophages. Primary sources of ROS after nerve damage are the mitochondria and
382 cellular NADPH oxidases. Studies in *ex vivo* cultured neurons indicate that Sarm1
383 acts downstream of mitochondrial ROS generation. Also, previous studies have
384 characterized Wallerian axon degeneration and regeneration in Erbb2 mutant
385 specimens, but did not address effects on the wound microenvironment and the
386 behavior of macrophages (93-94). Accordingly, tested *in vivo* if the loss of Sarm1 as
387 well as the absence of Schwann cells would affect macrophage recruitment, to find
388 that the onset of recruitment, the retention time and number of macrophages at the

389 wound did not differ between wild-type specimens and Sarm1 or Erbb2 mutants.
390 Also, as in wild-type specimens, macrophages in Sarm1 and Erbb2 mutants engulfed
391 debris locally, which were larger within macrophages in Ebbr2 mutants. Thus, the
392 loss of Sarm1 does not affect focal damage resolution by macrophages, which are
393 recruited and activated independently of the Schwann cells.
394

395 **CONCLUSIONS**

396 Current mechanistic details about Sarm1 function derive from independent
397 observations extrapolated from a wide variety of experimental systems. This has
398 made it difficult to synthetize findings and reconcile some conflicting observations.
399 Here, we have exploited a powerful *in vivo* genetic system to comprehensively study
400 the consequence of systemic loss of Sarm1 from the sub-cellular to the organismal
401 level in a single vertebrate system. By generating zebrafish carrying loss-of-function
402 mutations in Sarm1, we confirmed and deepen previous findings from *Drosophila*, the
403 mouse and cultured cells. Several novel insights derive from the work presented here.
404 First, that loss of Sarm1 is well tolerated by the animal. Second, that neuronal-circuit
405 repair is not contingent upon rapid clearance of damaged axons. Third, that
406 Schwann cells are not necessary for maintenance of severed axons *in vivo*. Fourth, that
407 after the axotomy Schwann cells distal to the cut site don't dedifferentiate in Sarm1-
408 mutants *in vivo*. Fifth, that the protracted maintenance of transected axons
409 dramatically improves Schwann-cell tolerance to chemotoxicity after nerve injury
410 after neurotrauma. This scenario is likely to occur in the clinical setting because nerve
411 trauma is an inescapable consequence of surgical interventions, chronic metabolic

412 dysfunction including diabetes, and pharmacological treatments such as antibiotics
413 and anæsthesia that increase cellular stress (81). Therefore, these findings are of
414 obvious pathophysiological significance. Crucially, these data lend strong support to
415 the idea that direct interventions to systemically inhibit axon degradation are
416 promising strategies to reduce chronic consequences of neurotrauma. Because TIR
417 domain dimerization is necessary and sufficient to degrade NAD+, it renders Sarm1
418 amenable to inhibition by small molecules, as it has been demonstrated for the TIR
419 domain of TLR2 (95). Our findings encourage the development of Sarm1 inhibitors
420 for therapeutic applications (18, 29).
421
422
423
424
425
426
427
428
429
430
431
432
433
434
435
436
437
438

439

440

441 **MATERIALS & METHODS**

442 **Zebrafish strains and husbandry**

443 Zebrafish (*Danio rerio*) were maintained in a centralized facility in accordance to
444 guidelines by the Ethical Committee of Animal Experimentation of the Helmholtz
445 Zentrum München, the German Animal Welfare act Tierschutzgesetz §11, Abs. 1,
446 Nr. 1, Haltungserlaubnis, to European Union animal welfare, and to protocols
447 number Gz.:55.2-1-54-2532-202-2014 and Gz.:55.2-2532.Vet_02-17-187 from the
448 "Regierung von Oberbayern", Germany. The transgenic lines Tg[UAS:EGFP],
449 Tg[HGn39D] and Tg[SILL:mCherry] (67), Tg[gSAGFF202A] (41),
450 Tg[UAS:GCaMP7a] (88), Tg[mbpa:tgRFP-CAAX]$^{tum102Tg}$ (also known as
451 Tg[MBP:tgRFP]) (89) and Erbb2 mutants (41, 59) have been previously published.
452 The Tg[Sarm1-/-] was generated by CRISPR/Cas9 mediated mutagenesis.

453 **Sarm1 mutagenesis**

454 We used CRISPR/Cas9-mediated genome modification to generate loss-of-function
455 mutations in exon 1 of Sarm1. Cas9 mRNA and sgRNAs were co-injected into one-
456 cell stage embryos. Cas9 mRNA was generated *in vitro* from PmeI linearized CAS9
457 vector (pMLM3613) using the Ambion™ mMESSAGE mMACHINE T7 Kit. The
458 mRNA was purified with the RNA easy kit (Qiagen). To generate the sgRNAs, the
459 target exon was sequenced and the sequence information was used to design
460 oligonucleotides for the sgRNA guide vector (pDR274) using the on-line tool "ZiFiT
461 Targeter software package" (http://zifit.partners.org/) (90). The sgRNA sequence
462 for exon 1 of Sarm1 is 5'-GGGACTTGGAAGAGACCCGC-3'. The annealed
463 oligonucleotide was cloned into the BsaI-digested pDR274 vector using T4 ligase
464 (NEB M0202). Resulting clones were sequenced to verify correctness, and then
465 linearized with DraI. The purified linearized DNA fragment was employed to
466 generate the sgRNA using the T7 MEGAscript kit (Ambion™). By out-crossing adult
467 fish resulting from injection, we obtained germ-line transmission of two independent
468 alleles: *sarm1*$^{hzm13}$ and *sarm1*$^{hzm14}$. For genotyping mutant carriers, we used the primers:

469 Forward: 5'-GATTTGCCGTTATCTCTCCA-3' and Reverse: 5'-
470 TCAAGCAGTTTGGCAGACTC-3'.

471 **DNA constructs**

472 The DNA constructs SILL:mCherry, SILL:Gal4 (67), UAS:Synapsin1-GFP (53) and
473 mbp:EGFP-CAAX have been previously described. The vectors pMLM3613 (42251)
474 and pDR272 (42250) were purchased from Addgene. The plasmids UAS:TRPV1-
475 tagRFP, the coding sequence of rat TRPV1 containing the E600K mutation fused
476 to tagRFP was commercially synthesized by Genecat and the expression construct
477 was generated using Tol2 kit. The constructs SILL:mito-mCherry, SILL:Sarm1-v2a-
478 mCherry, SILL:Kaede, SILL:mitoRGECO and SILL:erGCaMP3 were generated
479 using Tol2 kit. Mitochondria in lateralis neurons were marked by expressing the
480 mitochondria targeting sequence from the Cytochrome-C oxidase subunit 8A fused
481 to mCherry. The plasmids containing mito-RGECO and er-GCaMP3 (92) were a
482 gift of David W. Raible (University of Washington).

483 **Antibodies and immunostaining**

484 Whole-mount immunostaining was performed as following. First, samples of
485 zebrafish embryos or larvae were fixed by immersion in ice-cold 4%
486 paraformaldehyde diluted into phosphate-buffered saline buffer containing 0.2%
487 Tween20 (PBST), and incubated overnight at 4°C. Then, the samples were washed
488 at room temperature (RT) with PBST three times, 10 minutes per wash, and
489 subsequently blocked in 10% bovine serum albumin (BSA), also at RT for 1 hour.
490 Next, the samples were incubated in primary antibodies at 4°C overnight. Next, the
491 samples were washed in PBST for 2 hours, changing to fresh buffer every 30 minutes.
492 Finally, they were incubated with secondary antibodies at 4°C overnight. Primary
493 antibodies and concentrations: mouse anti-Acetylated tubulin, 1:1000 (Sigma T7251);
494 rat anti-Claudin-k, 1:500 (gift from T. Becker, University of Edinburgh, U.K.) (71);
495 mouse 6D2, 1:5 (gift from Dr. G. Jeserich, University of Osnabrück, Germany) (73).
496 Secondary antibodies used were at the following concentrations: donkey anti-Mouse
497 Alexa Fluor® 555, 1:200, Abcam ab150106; donkey anti-Rat IgG H&L (Alexa
498 Fluor® 647) pre-adsorbed, 1:200, Abcam ab150155). Samples were washed in PBST

499 for 30 minutes and mounted in Vectashield one day before microscopic examination.
500 Imaging of fixed samples was done with a laser-scanning confocal microscope (LSM
501 510, Carl Zeiss).

502 **Intravital microscopy**

503 For videomicroscopy, larvae were anesthetized with MS-222 (0.013% M/V) in
504 Danieau's and mounted in 0.8% low melting-point agarose on a 35mm glass-bottom
505 Petri dish. Samples were gently pressed against the glass using a hair-loop glued to
506 the tip of a glass pipette, as previously described. The agarose dome was immersed
507 in Danieau's with the anesthetic. Images of the axons and Schwann cells were
508 acquired using a spinning-disc microscope with a 40× air objective at 28.5°C (58). Z-
509 stacks were set to 0.8-1.2 μm intervals. Time intervals were 10 minute or 15 minute
510 per stack. The resulting raw data were processed, assembled and analyzed with
511 ImageJ.

512 **Western blot assay**

513 Wild-type and mutant larvae were anesthetized and killed 5 days-post-fertilization.
514 Samples were homogenized in ice-cold RIPA buffer (with protease inhibitor cocktail
515 from Roche (Cat.04693159001). After homogenization, the samples were incubated
516 on ice for 30 minutes for further lysis. The resulting lysate was centrifuged at 1200
517 rpm at 4°C, and the supernatant was taken for the BCA assay. The supernatant was
518 diluted in loading buffer and boiled at 99°C for 5 minutes. Next, the samples were
519 performed in the SDS-PAGE and transferred onto a PVDF membrane. After
520 blocking the membrane in 5% skimmed milk (diluted in PBST) for 1 hour, the
521 membrane was incubated with the primary antibody (rabbit anti-Sarm1, 1:500,
522 ANASPEC 55381; Mouse anti-β-Tubulin, 1:2000, Sigma T5168) at 4°C overnight.
523 The next day, the membrane was washed and incubated with HRP-labeled
524 secondary antibody (Peroxidase-Affini Pure Goat Anti-Mouse IgG (H+L), 1:10000,
525 Jackson Immuno Research 115035003; Peroxidase-Affini Pure Goat Anti-Rabbit
526 IgG (H+L), 1:10000, Jackson ImmunoResearch 115035144) for 1 hour. Images were
527 acquired by developing the membrane with ECL (Pierce™ ECL Western Blotting
528 Substrate, Thermo Fisher, 32109).

529 **Laser microsurgery**

530 To mark lateralis sensory neurons individually, DNA of the SILL:mCherry construct
531 was injected into eggs of Tg[HGn39D], Tg[HGn39D; Sarm1-/-],
532 Tg[SILL:mCherry; gSAGFF202A; UAS:EGFP] or Tg[SILL:mCherry ;
533 gSAGFF202A ; UAS:EGFP ; Sarm1-/-] zebrafish. Resulting larvae were selected
534 according to red-fluorescence in lateralis neurons. Selected samples were mounted
535 into agarose as described above, and their peripheral axons were targeted an
536 ultraviolet laser (350nm) using the iLasPulse system (Roper scientific AS, Evry,
537 France), as described previously. The laser beam was delivered using a 63x water-
538 immersion objective (50, 53, 58). The laser pulses were calibrated and applied to the
539 target area until a clear gap in the axons was visible. The samples were observed
540 again 1 hour post-injury (hpi) to confirm that the axons were completely transected.

541 **Quantification of mitochondrial density and motility**

542 To analyze mitochondria in sensory axons, we generated kymographs of mito-
543 mCherry fluorescent spots using the Multi-Kymograph tool of the Fiji software
544 (http://fiji.sc). The movement of mitochondria was determined by the slope of the
545 lines drawn over time, and the direction of movement was determined by the moving
546 mitochondria crossing the time line (vertical) in the kymographs. The data were
547 analyzed with Python scripts and the Graphpad Prism software.

548 **Calcium imaging**

549 For calcium imaging in lateralis neurons, Tg[SILL:Gal4; UAS:GCaMP7a] double-
550 transgenic larvae were anesthetized and mounted in 0.8% low melting-point agarose
551 on a 35mm glass-bottom Petri dish. Imaging was acquired through a 63x water-
552 immersion objective with an exposure time of 400 milliseconds. Laser-mediated axon
553 transection was done after the 4$^{th}$ imaging of the time series. Next, live
554 videomicroscopy was done for 2 minutes at a frame rate of 400 milliseconds at 28.5°C.
555 The raw data were analyzed with ImageJ. To quantify the calcium signal, the images
556 were processed to ImageJ. The region of interest (ROI) was selected and measured
557 the value with time point. GCaMP or RGECO intensity changes were calculated as
558 follows: $\Delta F/F0 = (F-F0)/F0$, where F0 is the value of the fluorescent signal before

559 axons were transected, and F is the value of the fluorescent signal with time point
560 after axon severing (92).

561 **Chemogenetics**

562 For chemogenetic experiments, we co-injected the SILL:Gal4 with UAS:mCherry or
563 UAS:ratTRPV1-tagRFP into the Tg[UAS:GCaMP7a] or Tg[HGn39D; Sarm1-/-].
564 The positive larva with SILL:Gal4; UAS:ratTRPV1-tagRFP; UAS:GCaMP7a
565 expression was used to activate TRPV1 channels in zebrafish by incubation in 5μM
566 capsaicin (Sigma, M2028) and subsequent live imaging for 1hour of the mounted and
567 anesthetized embryo. Images were acquired through a 63x water-immersion
568 objective with an exposure time of 400 milliseconds. For experiments with the Sarm1
569 mutant larvae, the HGn39D with SILL:mCherry or ratTRPV1-tagRFP positive
570 animals were laser axotomized. The larvae were treated with 10 μM capsaicin or
571 ethanol (1:1000, v/v) 2h after transection. 1.5h after capsaicin treatment, images
572 were taken by spinning disc microscopy.

573 **Behavioral assays**

574 For the touch-mediated escape response, 2dpf embryos were gently dechorionated
575 and kept in Danieau's solution at 28°C for at least 1 hour. Embryos were place into
576 a flat uncovered Petri dish containing Danieau's and were recorded with a high-speed
577 camera (NX4 series, Imaging solution, GmbH). Video recording was launched and
578 a randomly chosen embryo was touched with a blunt glass needle until it evoked a
579 reaction. Recordings were done under white-light illumination over 150 seconds at a
580 rate of 200 frames per second (fps). The swimming trajectories were obtained with
581 3D Particle Tracker plugin, ImageJ software. The further quantification and statistics
582 were using Python.

583 **Statistical analysis**

584 The Student's t test (two tailed), one-way ANOVA test and Wilcoxon rank sum test
585 were applied using Python scripts. Error bars in all figures are standard errors of the
586 mean (SEM).

587

588

589

590 **REFERENCES**

591


592 1. Ameh V, and Crane S. Nerve injury following shoulder dislocation: the
593 emergency physician's perspective. *Eur J Emerg Med.* 2006;13(4):233-5.
594 2. Heneka MT, Carson MJ, El Khoury J, Landreth GE, et al. Neuroinflammation
595 in Alzheimer's disease. *Lancet Neurol.* 2015;14(4):388-405.
596 3. Missios S, Bekelis K, and Spinner RJ. Traumatic peripheral nerve injuries in
597 children: epidemiology and socioeconomics. *J Neurosurg Pediatr.* 2014;14:688-94.
598 4. Rowe RK, Ellis GI, Harrison JL, Bachstetter AD, et al. Diffuse traumatic brain
599 injury induces prolonged immune dysregulation and potentiates hyperalgesia
600 following a peripheral immune challenge. *Mol Pain.* 2016;12.
601 5. Tzekov R, Phifer J, Myers A, Mouzon B, and Crawford F. Inflammatory
602 changes in optic nerve after closed-head repeated traumatic brain injury:
603 Preliminary study. *Brain Inj.* 2016;30(12):1428-35.
604 6. Ziogas NK, and Koliatsos VE. Primary Traumatic Axonopathy in Mice
605 Subjected to Impact Acceleration: A Reappraisal of Pathology and
606 Mechanisms with High-Resolution Anatomical Methods. *J Neurosci.* 2018;
607 38:4031-47.
608 7. Roselli F, and Caroni P. From intrinsic firing properties to selective neuronal
609 vulnerability in neurodegenerative diseases. *Neuron.* 2015;85(5):901-10.
610 8. Cattin AL, and Lloyd AC. The multicellular complexity of peripheral nerve
611 regeneration. *Curr Opin Neurobiol.* 2016;39:38-46.
612 9. Parrinello S, Napoli I, Ribeiro S, Wingfield Digby P, Fedorova M, Parkinson
613 DB, et al. EphB signaling directs peripheral nerve regeneration through Sox2-
614 dependent Schwann cell sorting. *Cell.* 2010;143(1):145-55.
615 10. Ziegenfuss JS, Doherty J, and Freeman MR. Distinct molecular pathways
616 mediate glial activation and engulfment of axonal debris after axotomy. *Nat*
617 *Neurosci.* 2012;15(7):979-87.
618 11. Harrisingh MC, Pérez-Nadales E, Parkinson DB, Malcolm DS, Mudge AW,
619 and Lloyd AC. The Ras/Raf/ERK signalling pathway drives Schwann cell
620 dedifferentiation. *EMBO J.* 2004;23(15):3061-71.
621 12. Scherer SS. The biology and pathobiology of Schwann cells. *Curr Opin Neurol.*
622 1997;10(5):386-97.
623 13. Waller A. Experiments on the Section of the Glossopharyngeal and
624 Hypoglossal Nerves of the Frog, and Observations of the Alterations Produced
625 Thereby in the Structure of Their Primitive Fibres. *Philosophical Transactions of*
626 *the Royal Society of London.*140:423-9
627 14. Gerdts J, Summers DW, Milbrandt J, and DiAntonio A. Axon Self-
628 Destruction: New Links among SARM1, MAPKs, and NAD+ Metabolism.
629 *Neuron.* 2016;89(3):449-60.
630 15. Osterloh JM, Yang J, Rooney TM, Fox AN, Adalbert R, Powell EH, et al.
631 dSarm/Sarm1 is required for activation of an injury-induced axon death
632 pathway. *Science.* 2012;337(6093):481-4.

633 16. Walker LJ, Summers DW, Sasaki Y, Brace EJ, Milbrandt J, and DiAntonio A.
634 MAPK signaling promotes axonal degeneration by speeding the turnover of the
635 axonal maintenance factor NMNAT2. *Elife.* 2017;6.
636 17. Yang J, Wu Z, Renier N, Simon DJ, et al. Pathological axonal death through a
637 MAPK cascade that triggers a local energy deficit. *Cell.* 2015;160:161-76.
638 18. Essuman K, Summers DW, Sasaki Y, Mao X, DiAntonio A, and Milbrandt J.
639 The SARM1 Toll/Interleukin-1 Receptor Domain Possesses Intrinsic NAD(+)
640 Cleavage Activity that Promotes Pathological Axonal Degeneration. *Neuron.*
641 2017;93(6):1334-43 e5.
642 19. Gerdts J, Summers DW, Sasaki Y, DiAntonio A, and Milbrandt J. Sarm1-
643 mediated axon degeneration requires both SAM and TIR interactions. *J*
644 *Neurosci.* 2013;33(33):13569-80.
645 20. Gerdts J, Brace EJ, Sasaki Y, DiAntonio A, and Milbrandt J. SARM1
646 activation triggers axon degeneration locally via NAD(+) destruction. *Science.*
647 2015;348(6233):453-7.
648 21. Loreto A, Di Stefano M, Gering M, and Conforti L. Wallerian Degeneration Is
649 Executed by an NMN-SARM1-Dependent Late Ca(2+) Influx but Only
650 Modestly Influenced by Mitochondria. *Cell Rep.* 2015;13(11):2539-52.
651 22. Summers DW, Gibson DA, DiAntonio A, and Milbrandt J. SARM1-specific
652 motifs in the TIR domain enable NAD+ loss and regulate injury-induced
653 SARM1 activation. *Proc Natl Acad Sci U S A.* 2016;113(41):E6271-E80.
654 23. Essuman K, Summers DW, Sasaki Y, Mao X, Yim AKY, DiAntonio A, et al.
655 TIR Domain Proteins Are an Ancient Family of NAD(+)-Consuming
656 Enzymes. *Curr Biol.* 2018;28(3):421-30 e4.
657 24. Sasaki Y, Nakagawa T, Mao X, DiAntonio A, and Milbrandt J. NMNAT1
658 inhibits axon degeneration via blockade of SARM1-mediated NAD(+)
659 depletion. *Elife.* 2016;5.
660 25. Jessen KR, Mirsky R, and Lloyd AC. Schwann Cells: Development and Role
661 in Nerve Repair. *Cold Spring Harb Perspect Biol.* 2015;7(7):a020487.
662 26. Jortner BS. Mechanisms of toxic injury in the peripheral nervous system:
663 neuropathologic considerations. *Toxicol Pathol.* 2000;28(1):54-69.
664 27. Morell P, and Toews AD. Schwann cells as targets for neurotoxicants.
665 *Neurotoxicology.* 1996;17(3-4):685-95.
666 28. Koeppen AH. Wallerian degeneration: history and clinical significance. *J Neurol*
667 *Sci.* 2004;220(1-2):115-7.
668 29. Simon DJ, and Watkins TA. Therapeutic opportunities and pitfalls in the
669 treatment of axon degeneration. *Curr Opin Neurol.* 2018;31(6):693-701.
670 30. Schuldiner O, and Yaron A. Mechanisms of developmental neurite pruning.
671 *Cell Mol Life Sci.* 2015;72(1):101-19.
672 31. Omura T, Omura K, Tedeschi A, Riva P, et al. Robust Axonal Regeneration
673 Occurs in the Injured CAST/Ei Mouse CNS. *Neuron.* 2015;86(5):1215-27.
674 32. D'Rozario M, Monk KR, and Petersen SC. Analysis of myelinated axon
675 formation in zebrafish. *Methods Cell Biol.* 2017;138:383-414.
676 33. Friedrich RW, Genoud C, and Wanner AA. Analyzing the structure and
677 function of neuronal circuits in zebrafish. *Front Neural Circuits.* 2013;7:71.

678 34. Friedrich RW, Jacobson GA, and Zhu P. Circuit neuroscience in zebrafish.
679 *Curr Biol.* 2010;20(8):R371-81.
680 35. Ackerman SD, Garcia C, Piao X, Gutmann DH, and Monk KR. The adhesion
681 GPCR Gpr56 regulates oligodendrocyte development via interactions with
682 Galpha12/13 and RhoA. *Nat Commun.* 2015;6:6122.
683 36. Bin JM, and Lyons DA. Imaging Myelination In Vivo Using Transparent
684 Animal Models. *Brain Plast.* 2016;2(1):3-29.
685 37. Fontenas L, and Kucenas S. Livin' On The Edge: glia shape nervous system
686 transition zones. *Curr Opin Neurobiol.* 2017;47:44-51.
687 38. Ohki Y, Wenninger-Weinzierl A, Hruscha A, Asakawa K, Haass C, et al.
688 Glycine-alanine dipeptide repeat protein contributes to toxicity in a zebrafish
689 model of C9orf72 associated neurodegeneration. *Mol Neurodegener.* 2017;12(1):6.
690 39. Rosenberg AF, Isaacman-Beck J, Franzini-Armstrong C, and Granato M.
691 Schwann cells and deleted in colorectal carcinoma direct regenerating motor
692 axons towards their original path. *J Neurosci.* 2014;34(44):14668-81.
693 40. Wehner D, Tsarouchas TM, Michael A, Haase C, Weidinger G, Reimer MM,
694 et al. Wnt signaling controls pro-regenerative Collagen XII in functional spinal
695 cord regeneration in zebrafish. *Nat Commun.* 2017;8(1):126.
696 41. Xiao Y, Faucherre A, Pola-Morell L, Heddleston JM, Liu TL, Chew TL, et al.
697 High-resolution live imaging reveals axon-glia interactions during peripheral
698 nerve injury and repair in zebrafish. *Dis Model Mech.* 2015;8(6):553-64.
699 42. O'Donnell KC, Vargas ME, and Sagasti A. WldS and PGC-1alpha regulate
700 mitochondrial transport and oxidation state after axonal injury. *J Neurosci.*
701 2013;33(37):14778-90.
702 43. Conforti L, Gilley J, and Coleman MP. Wallerian degeneration: an emerging
703 axon death pathway linking injury and disease. *Nat Rev Neurosci.* 2014;15:394.
704 44. Howe K, Clark MD, Torroja CF, Torrance J, Berthelot C, Muffato M, et al.
705 The zebrafish reference genome sequence and its relationship to the human
706 genome. *Nature.* 2013;496(7446):498-503.
707 45. Sztal TE, Ruparelia AA, Williams C, and Bryson-Richardson RJ. Using
708 Touch-evoked Response and Locomotion Assays to Assess Muscle
709 Performance and Function in Zebrafish. *J Vis Exp.* 2016(116).
710 46. Ghysen A, and Dambly-Chaudière C. The lateral line microcosmos. *Genes Dev.*
711 2007;21(17):2118-30.
712 47. Pujol-Martí J, and López-Schier H. Developmental and architectural principles
713 of the lateral-line neural map. *Front Neural Circuits.* 2013;7:47.
714 48. Drerup CM, and Nechiporuk AV. In vivo analysis of axonal transport in
715 zebrafish. *Methods Cell Biol.* 2016;131:311-29.
716 49. Haehnel-Taguchi M, Akanyeti O, and Liao JC. Behavior, Electrophysiology,
717 and Robotics Experiments to Study Lateral Line Sensing in Fishes. *Integr Comp*
718 *Biol.* 2018;58(5):874-83.
719 50. Pujol-Martí J, Faucherre A, Aziz-Bose R, Asgharsharghi A, Colombelli J,
720 Trapani JG, et al. Converging axons collectively initiate and maintain synaptic
721 selectivity in a constantly remodeling sensory organ. *Curr. Biol.*
722 2014;24(24):2968-74.

723 51. Olt J, Ordoobadi AJ, Marcotti W, and Trapani JG. Physiological recordings
724 from the zebrafish lateral line. *Methods Cell Biol.* 2016;133:253-79.
725 52. Vargas ME, Yamagishi Y, Tessier-Lavigne M, and Sagasti A. Live Imaging of
726 Calcium Dynamics during Axon Degeneration Reveals Two Functionally
727 Distinct Phases of Calcium Influx. *J Neurosci.* 2015;35(45):15026-38.
728 53. Xiao Y, Tian W, and Lopez-Schier H. Optogenetic stimulation of neuronal
729 repair. *Curr Biol.* 2015;25(22):R1068-9.
730 54. Kim MJ, Kang KH, Kim CH, and Choi SY. Real-time imaging of
731 mitochondria in transgenic zebrafish expressing mitochondrially targeted GFP.
732 *Biotechniques.* 2008;45(3):331-4.
733 55. Mandal A, Pinter K, and Drerup CM. Analyzing Neuronal Mitochondria *in*
734 *vivo* Using Fluorescent Reporters in Zebrafish. *Front Cell Dev Biol.* 2018;6:144.
735 56. Lin MY, Cheng XT, Tammineni P, Xie Y, Zhou B, Cai Q, et al. Releasing
736 Syntaphilin Removes Stressed Mitochondria from Axons Independent of
737 Mitophagy under Pathophysiological Conditions. *Neuron.* 2017;94:595-610 e6.
738 57. Miller KE, and Sheetz MP. Axonal mitochondrial transport and potential are
739 correlated. *J Cell Sci.* 2004;117(Pt 13):2791-804.
740 58. Xiao Y, and López-Schier H. Studying Axonal Regeneration by Laser
741 Microsurgery and High-Resolution Videomicroscopy. *Methods Mol Biol.*
742 2016;1451:271-80.
743 59. Lyons DA, Pogoda HM, Voas MG, Woods IG, Diamond B, Nix R, et al.
744 erbb3 and erbb2 are essential for schwann cell migration and myelination in
745 zebrafish. *Curr Biol.* 2005;15(6):513-24.
746 60. Ozaki T, Yamashita T, and Ishiguro S. Mitochondrial m-calpain plays a role in
747 the release of truncated apoptosis-inducing factor from the mitochondria.
748 *Biochim Biophys Acta.* 2009;1793(12):1848-59.
749 61. Court FA, and Coleman MP. Mitochondria as a central sensor for axonal
750 degenerative stimuli. *Trends Neurosci.* 2012;35(6):364-72.
751 62. Villegas R, Martinez NW, Lillo J, Pihan P, Hernandez D, Twiss JL, et al.
752 Calcium release from intra-axonal endoplasmic reticulum leads to axon
753 degeneration through mitochondrial dysfunction. *J Neurosci.* 2014;34:7179-89.
754 63. Park JY, Jang SY, Shin YK, Suh DJ, and Park HT. Calcium-dependent
755 proteasome activation is required for axonal neurofilament degradation. *Neural*
756 *Regen Res.* 2013;8(36):3401-9.
757 64. Caterina MJ, Schumacher MA, Tominaga M, Rosen TA, Levine JD, and
758 Julius D. The capsaicin receptor: a heat-activated ion channel in the pain
759 pathway. *Nature.* 1997;389(6653):816-24.
760 65. Gau P, Poon J, Ufret-Vincenty C, Snelson CD, Gordon SE, Raible DW, et al.
761 The zebrafish ortholog of TRPV1 is required for heat-induced locomotion. *J*
762 *Neurosci.* 2013;33(12):5249-60.
763 66. Brosius LA, and Barres BA. Contrasting the glial response to axon injury in the
764 central and peripheral nervous systems. *Dev. Cell.* 2014;28(1):7-17.
765 67. Faucherre A, Pujol-Martí J, Kawakami K, and López-Schier H. Afferent
766 neurons of the zebrafish lateral line are strict selectors of hair-cell orientation.
767 *PLoS One.* 2009;4(2):e4477.

768 68. Sasaki Y, Hackett AR, Kim S, Strickland A, and Milbrandt J. Dysregulation of
769 NAD(+) Metabolism Induces a Schwann Cell Dedifferentiation Program. *J*
770 *Neurosci.* 2018;38(29):6546-62.
771 69. Soto J, and Monje PV. Axon contact-driven Schwann cell dedifferentiation.
772 *Glia.* 2017;65(6):864-82.
773 70. Carr MJ, and Johnston AP. Schwann cells as drivers of tissue repair and
774 regeneration. *Curr Opin Neurobiol.* 2017;47:52-7.
775 71. Munzel EJ, Schaefer K, Obirei B, Kremmer E, Burton EA, Kuscha V, et al.
776 Claudin k is specifically expressed in cells that form myelin during development
777 of the nervous system and regeneration of the optic nerve in adult zebrafish.
778 *Glia.* 2012;60(2):253-70.
779 72. López-Schier H, and Hudspeth AJ. Supernumerary neuromasts in the
780 posterior lateral line of zebrafish lacking peripheral glia. *Proc Natl Acad Sci U S A.*
781 2005;102(5):1496-501.
782 73. Bastmeyer M, Jeserich G, and Stuermer CA. Similarities and differences
783 between fish oligodendrocytes and Schwann cells in vitro. *Glia.* 1994;11:300-14.
784 74. Czopka T, Ffrench-Constant C, and Lyons DA. Individual oligodendrocytes
785 have only a few hours in which to generate new myelin sheaths in vivo. *Dev Cell.*
786 2013;25(6):599-609.
787 75. Cavaletti G, Alberti P, and Marmiroli P. Chemotherapy-induced peripheral
788 neurotoxicity in the era of pharmacogenomics. *Lancet Oncol.* 2011;12:1151-61.
789 76. Kaiser J, Bledowski C, and Dietrich J. Neural correlates of chemotherapy-
790 related cognitive impairment. *Cortex.* 2014;54:33-50.
791 77. McLeary F, Davis A, Rudrawar S, Perkins A, and Anoopkumar-Dukie S.
792 Mechanisms underlying select chemotherapeutic-agent-induced
793 neuroinflammation and subsequent neurodegeneration. *Eur J Pharmacol.*
794 2018;842:49-56.
795 78. Fukuda Y, Li Y, and Segal RA. A Mechanistic Understanding of Axon
796 Degeneration in Chemotherapy-Induced Peripheral Neuropathy. *Front Neurosci.*
797 2017;11:481.
798 79. Gornstein E, and Schwarz TL. The paradox of paclitaxel neurotoxicity:
799 Mechanisms and unanswered questions. *Neuropharmacology.* 2014;76:175-83.
800 80. Imai S, Koyanagi M, Azimi Z, Nakazato Y, Matsumoto M, Ogihara T, et al.
801 Taxanes and platinum derivatives impair Schwann cells via distinct
802 mechanisms. *Sci Rep.* 2017;7(1):5947.
803 81. Yang S, Abrahams MS, Hurn PD, Grafe MR, Kirsch JR. Local anesthetic
804 Schwann cell toxicity is time and concentration dependent. *Reg Anesth Pain Med.*
805 2011;36:444-51.
806 82. Bremer J, Skinner J, and Granato M. A small molecule screen identifies *in vivo*
807 modulators of peripheral nerve regeneration in zebrafish. *PLoS One.*
808 2017;12(6):e0178854.
809 83. Gilley J, Ribchester RR, and Coleman MP. Sarm1 Deletion, but Not Wld(S),
810 Confers Lifelong Rescue in a Mouse Model of Severe Axonopathy. *Cell Rep.*
811 2017;21:10-6.

812 84. Henninger N, Bouley J, Sikoglu EM, An J, Moore CM, King JA, et al.
813 Attenuated traumatic axonal injury and improved functional outcome after
814 traumatic brain injury in mice lacking Sarm1. *Brain.* 2016;139(Pt 4):1094-105.
815 85. Geisler S, Doan RA, Strickland A, Huang X, Milbrandt J, and DiAntonio A.
816 Prevention of vincristine-induced peripheral neuropathy by genetic deletion of
817 SARM1 in mice. *Brain.* 2016;139(Pt 12):3092-108.
818 86. Turkiew E, Falconer D, Reed N, and Hoke A. Deletion of Sarm1 gene is
819 neuroprotective in two models of peripheral neuropathy. *J Peripher Nerv Syst.*
820 2017;22(3):162-71.
821 87. Clements MP, Byrne E, Camarillo Guerrero LF, Cattin AL, Zakka L, Ashraf
822 A, et al. The Wound Microenvironment Reprograms Schwann Cells to
823 Invasive Mesenchymal-like Cells to Drive Peripheral Nerve Regeneration.
824 *Neuron.* 2017;96(1):98-114 e7.
825 88. Muto A, Ohkura M, Abe G, Nakai J, and Kawakami K. Real-time
826 visualization of neuronal activity during perception. *Curr Biol.* 2013;23:307-11.
827 89. Auer F, Vagionitis S, and Czopka T. Evidence for Myelin Sheath Remodeling
828 in the CNS Revealed by In Vivo Imaging. *Curr Biol.* 2018;28(4):549-59 e3.
829 90. Wright DA, Thibodeau-Beganny S, Sander JD, Winfrey RJ, Hirsh AS,
830 Eichtinger M, et al. Standardized reagents and protocols for engineering zinc
831 finger nucleases by modular assembly. *Nat Protoc.* 2006;1(3):1637-52.
832 91. Czopka T, and Lyons DA. Individual oligodendrocytes have only a few hours
833 in which to generate new myelin sheaths *in vivo*. *Dev. Cell.* 2013;25(6):599-609.
834 92. Esterberg R, Linbo T, Pickett SB, Wu P, Ou HC, Rubel EW, et al.
835 Mitochondrial calcium uptake underlies ROS generation during
836 aminoglycoside-induced hair cell death. *J Clin Invest.* 2016;126(9):3556-66.
837 93. Atanasoski, S., Scherer, S. S., Sirkowski, E., Leone, D., Garratt, A. N.,
838 Birchmeier, C., & Suter, U. ErbB2 signaling in Schwann cells is mostly
839 dispensable for maintenance of myelinated peripheral nerves and proliferation
840 of adult Schwann cells after injury. *J. Neurosci.* 2006; 26: 2124-31.
841 94. Han, S. B., Kim, H., Lee, H., Grove, M., Smith, G. M., & Son, Y. J. Postinjury
842 induction of activated ErbB2 selectively hyperactivates denervated Schwann
843 cells and promotes robust dorsal root axon regeneration. *J. Neurosci.* 2017; 37:
844 10955–10970.
845 95. Mistry P, Laird MH, Schwarz RS, Greene S, Dyson T, Snyder GA, et al.
846 Inhibition of TLR2 signaling by small molecule inhibitors targeting a pocket
847 within the TLR2 TIR domain. *Proc. Natl. Acad. Sci. U.S.A.* 2015; 112:5455-60.
848

849

850

851

852

853

854 **FIGURE LEGENDS**

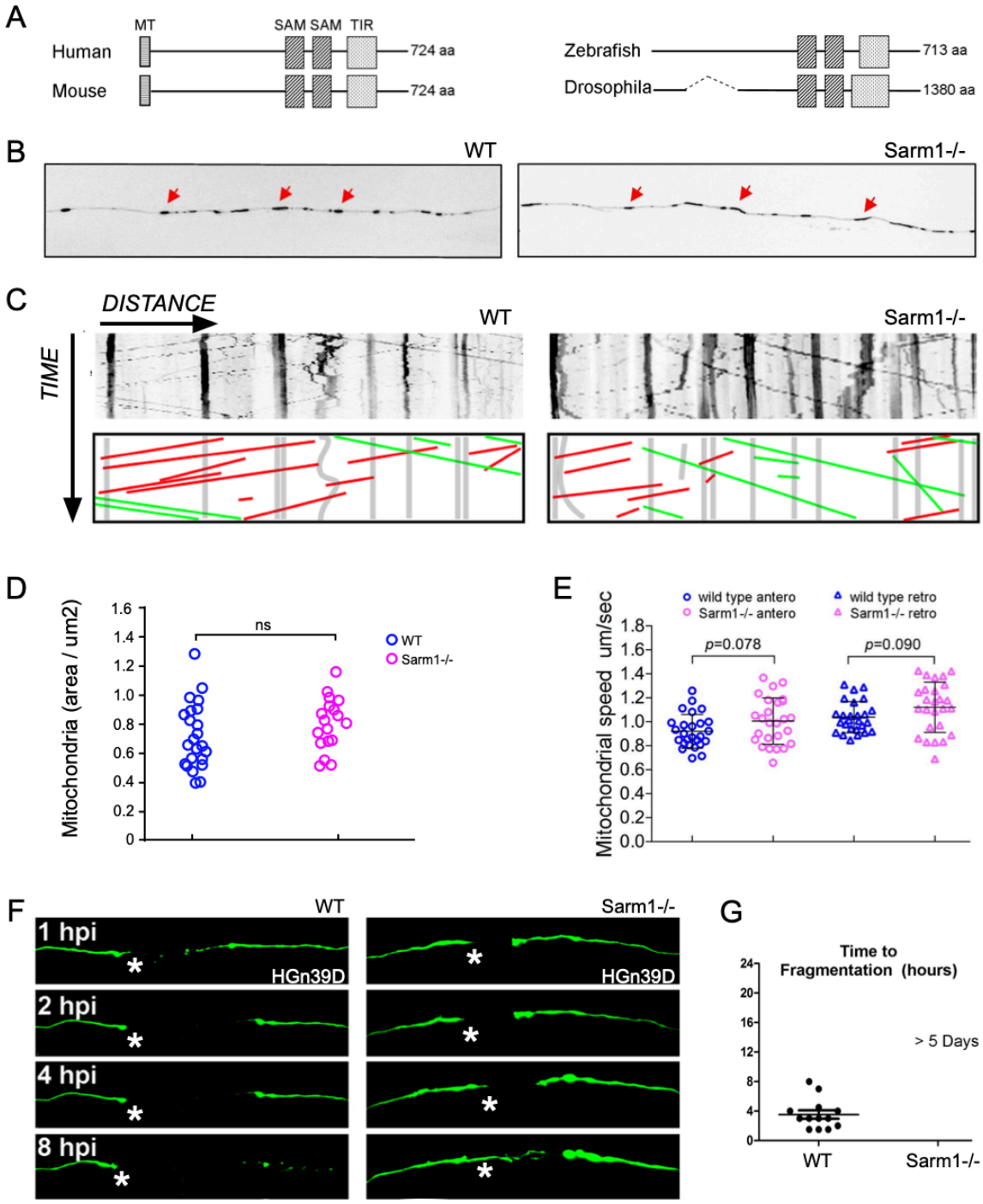


855

856 **Figure 1. A)** Structure Sarm1 indicating alignment of the Sarm1 functional domains
857 from different species (not at scale). **B)** Confocal image of axonal mitochondria
858 marked with mito-mCherry in wild-type and Sarm1-/-. Red arrows point to
859 prominent mitochondrial groups in axons. **C)** Upper panels, kymographs from
860 videomicroscopic recording of axonal mitochondria in wild type (H) (left panel) and

861 Sarm1-/- (I) (right panel). Lower panels show color-coded traces of moving
862 mitochondria in anterograde (green) and retrograde (red) directions, taken from the
863 kymographs shown in the upper panels. **D)** Density of mitochondria in 5dpf wild
864 type and Sarm1-/-, Error bar = SEM; n.s. = not significant, p value from Student's
865 t test, n=25 (WT), n=19 (Sarm1-/-). **E)** Mobility of the mitochondria in 5dpf wild
866 type and Sarm1-/-. Circles show the anterograde and triangles the retrograde
867 movement of the mitochondria. p value from one-way ANOVA, wild type n=26,
868 Sarm1-/- n=26. **F)** Time-lapse images of axonal degeneration of GFP-labeled
869 lateralis sensory neuron in wild-type (left) and Sarm1-/- larvae (right). hpi = hour
870 post injury, scale bar=50µm, white asterisk indicates the regrowing axons from the
871 proximal stump. **G)** Quantification of the time from axon transection to
872 fragmentation in wild type (n=13) and Sarm1-/- (n=13).
873
874

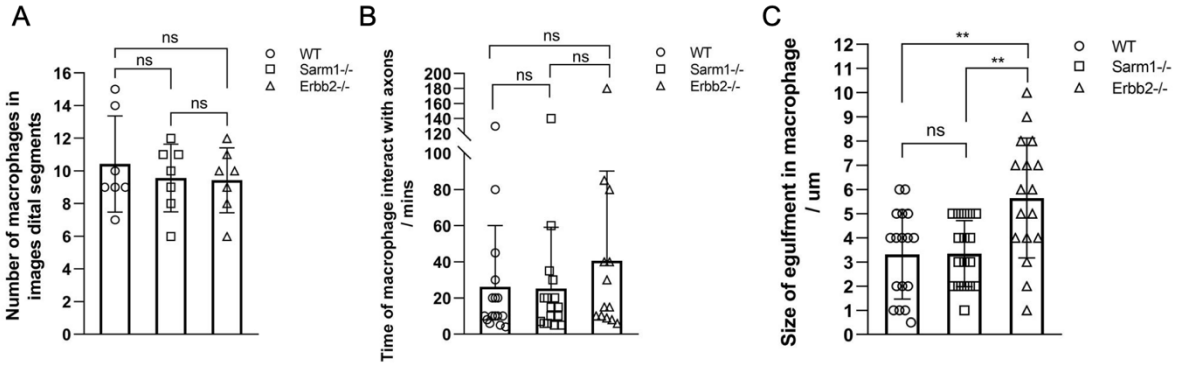


875
876 **Figure 2. A)** Quantification of the number of macrophages recruited to the injury
877 site and adjacent axon segments. **B)** Quantification of the time macrophages interact
878 with axon segments. **C)** Quantification of the size of debris within macrophages. P
879 values for T-test.
880

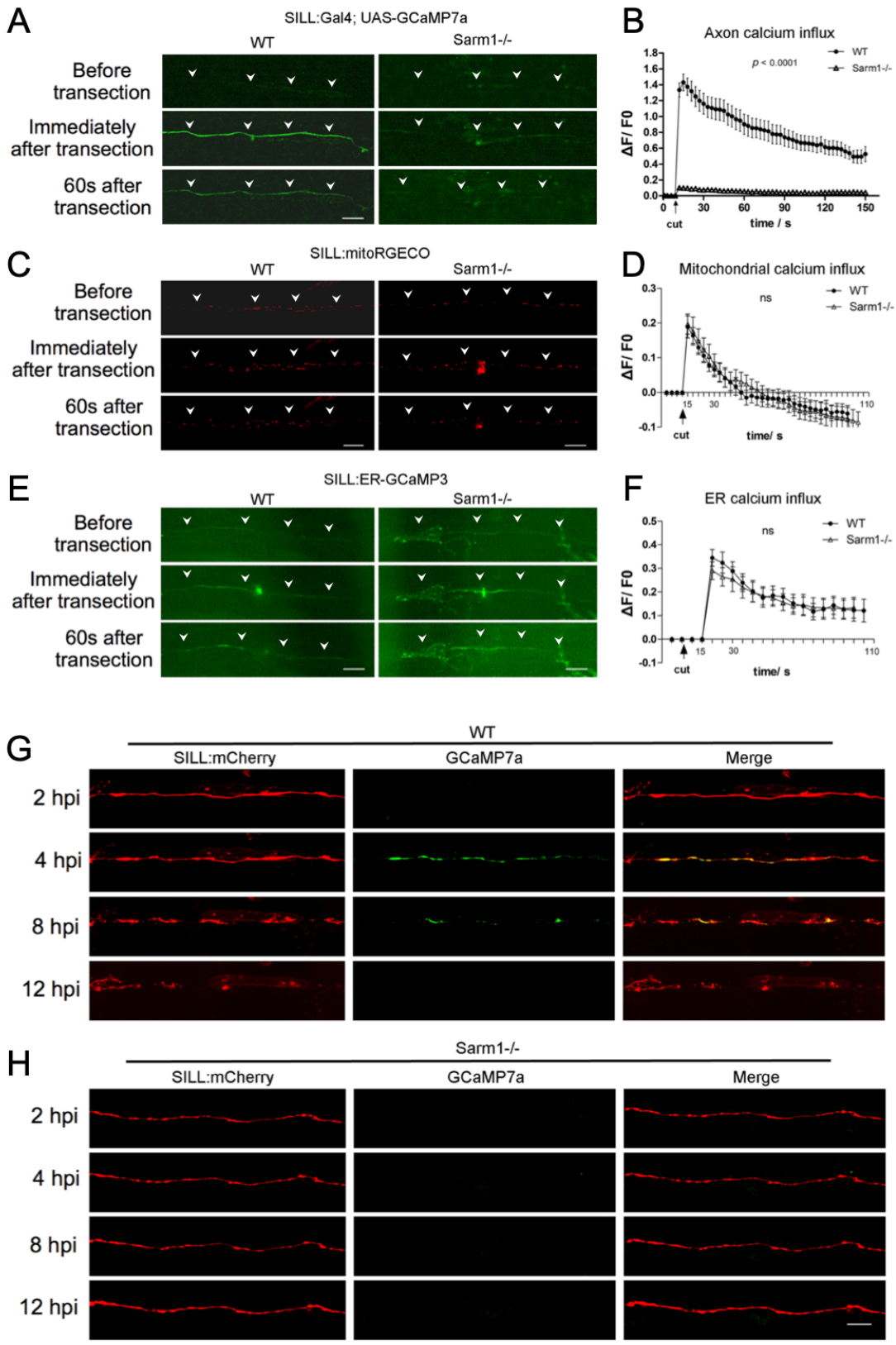


**Figure 3. A)** Confocal image of a single lateralis sensory axon expressing the green-fluorescent calcium sensor GCaMP7a in wild type (left column) and Sarm1-/- fish

884 (right column). Rows show that same samples before laser-mediated transection (top),
885 immediately after transection (middle) and 60 seconds after transection (bottom). In
886 A, C and E, white arrowheads indicate the position of the axon, specifically when
887 signal-to-background is low. Scale bar 20μm. **B)** Shows quantification of the first
888 wave of axoplasmic calcium. Data are shown as mean ± SEM; p from one-way
889 ANOVA, wild type n = 16, Sarm1-/- 16. **C)** Shows a confocal image of lateralis
890 sensory axons expressing the red-fluorescent calcium sensor RGECO in wild type
891 (left column) and Sarm1-/- fish (right column). Rows show that same samples before
892 laser-mediated transection (top), immediately after transection (middle), and 60
893 seconds after transection (bottom). **D)** Quantification mitochondrial calcium influx
894 shows the strong and nearly identical elevation and decay in wild type and Sarm1-/-
895 immediately after the cuts. Data are shown as mean ± SEM; p from one-way
896 ANOVA, wild type n = 16, Sarm1-/- 16. **E)** Shows a confocal image of lateralis
897 sensory axons expressing the green-fluorescent calcium sensor CCaMP3 targeted to
898 the endoplasmic reticulum (ER) in wild type (left column) and Sarm1-/- fish (right
899 column). Rows show that same samples before laser-mediated transection (top),
900 immediately after transection (middle), and 60 seconds after transection (bottom). **F)**
901 Quantification ER calcium influx shows strong and statistically equal elevation and
902 decay in wild type and Sarm1-/- after the cuts. Data are shown as mean ± SEM; p
903 from one-way ANOVA, wild type n = 16, Sarm1-/- 16. **G)** Confocal image of a
904 lateralis sensory axons expressing the mCherry (red) and green-fluorescent calcium
905 sensor GCaMP7a (green) in wild type fish. Rows show same axons 2, 4, 8 and 12
906 hours after transection (hours-post-injury = hpi). **H)** Confocal image of lateralis
907 sensory axons expressing the mCherry (red) and green-fluorescent calcium sensor
908 GCaMP7a (green) in Sarm1-/- fish. Scale bar 20μm.
909

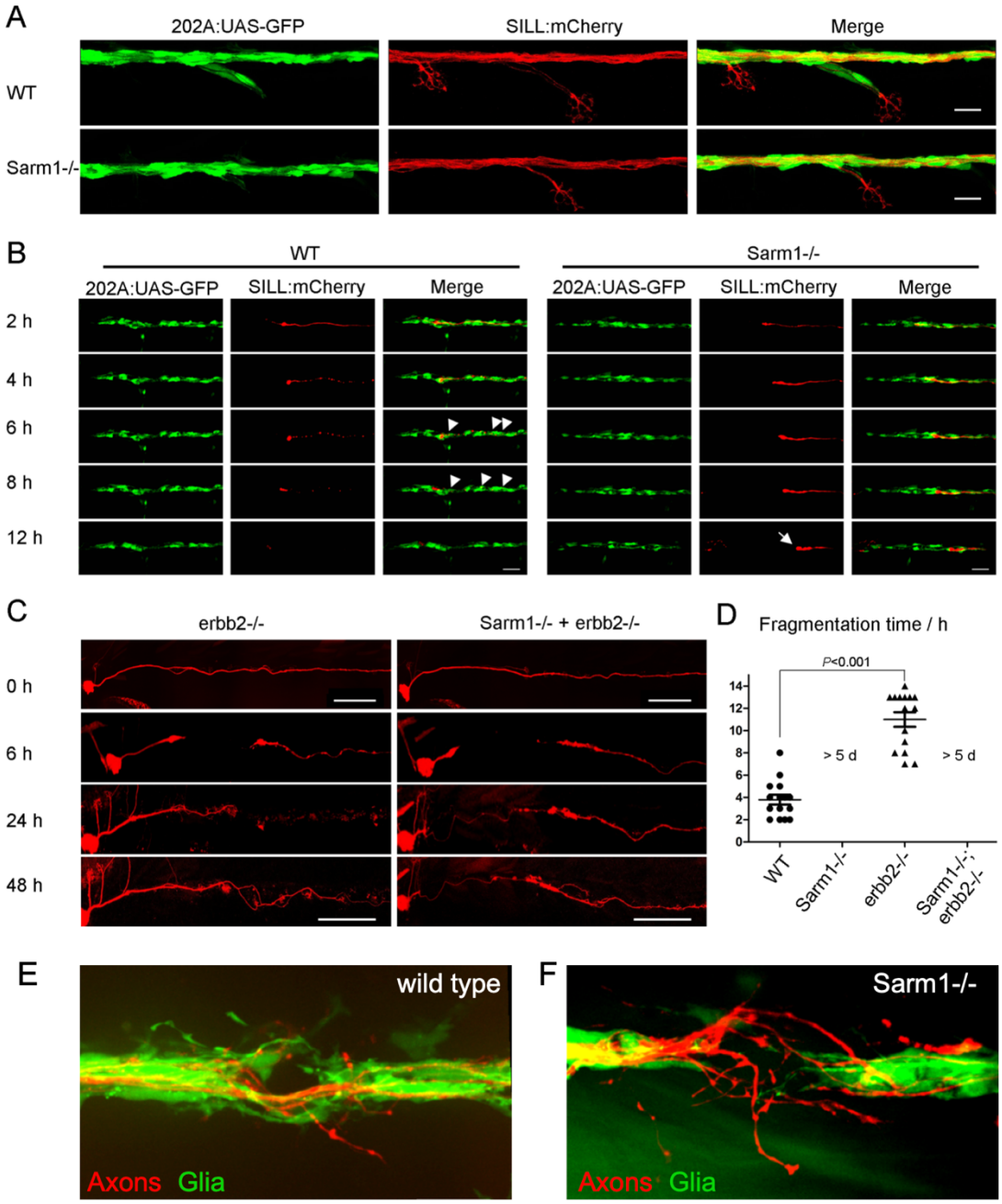


**Figure 4. A)** Confocal images of a double transgenic 5dpf larva showing Schwann cells marked by expression of GFP (green) under the control of the Tg[gSAGFF202A] Gal4 driver, and lateralis afferent neurons marked by expression of mCherry under the control of the SILL enhancer (red). Wild type (top), Sarm1 mutants (bottom). Scale bar 20µm. **B)** Images show the indicated time points after axon transection (hours post injury = hpi) from a videomicroscopic recording of Schwann cells (green) and their interaction with axons (red) in wild-type and Sarm1-/-. White arrowheads indicate Schwann cells engulfing axonal debris in the wild type.

919 A white arrow indicates degradation-resistant axon segment in Sarm1-/-. Please,
920 note that the proximal axon stump in Sarm1-/- is not visible in these images because
921 it is outside the focal plane. **C)** Images of mCherry-expressing (red) transected axons
922 in Erbb2-/- mutants and Sarm1-/- ; ErBb2-/- double mutants. Scale bar 100μm. **D)**
923 Quantification of transected axon fragmentation in Erbb2-/- and Sarm1-/-; ErBb2-
924 /-. Error bar = SEM, p value from One-way ANOVA test, n = 15 (each group). **E)**
925 Image of a from Supplemental Movie 1, showing the discrete local defasciculation of
926 regenerated the sensory fiber (red) and the bridging of the glial gap by Schwann cells
927 (green) in a wild-type specimen. **F)** Equivalent experiment, taken from Supplemental
928 Movie 2, showing a more pronounced local defasciculation of the regenerated the
929 sensory fiber (red) in a Sarm1-mutant specimen. Note that and the bridging of the
930 glial gap does not occur.
931
932

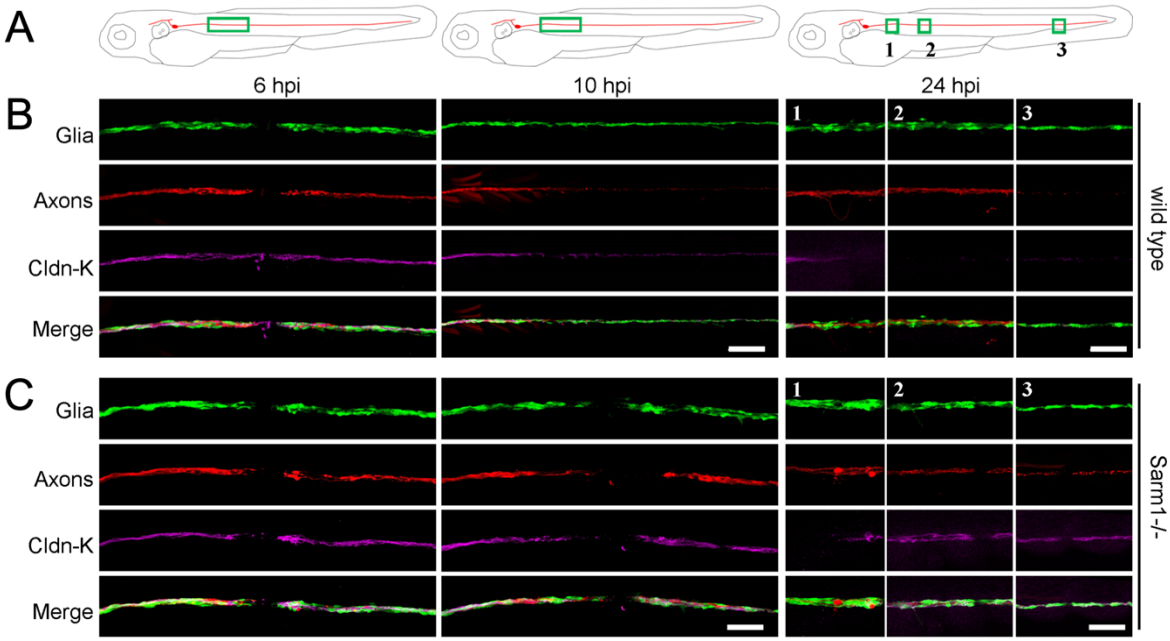


933
934 **Figure 5. A-C)** Schematic model of the confocal imaging locations on severed axons
935 (A). Confocal images of wild type (B) and Sarm1-/- (C) specimens in 6hpi, 10hpi and
936 24hpi. hpi = hour post injury. The specimens were the
937 Tg[gSAGFF202A;UAS:EGFP; SILL:mCherry] lines and were stained with Claudin-
938 k (magenta) antibody. Scale bar 50μm.

939

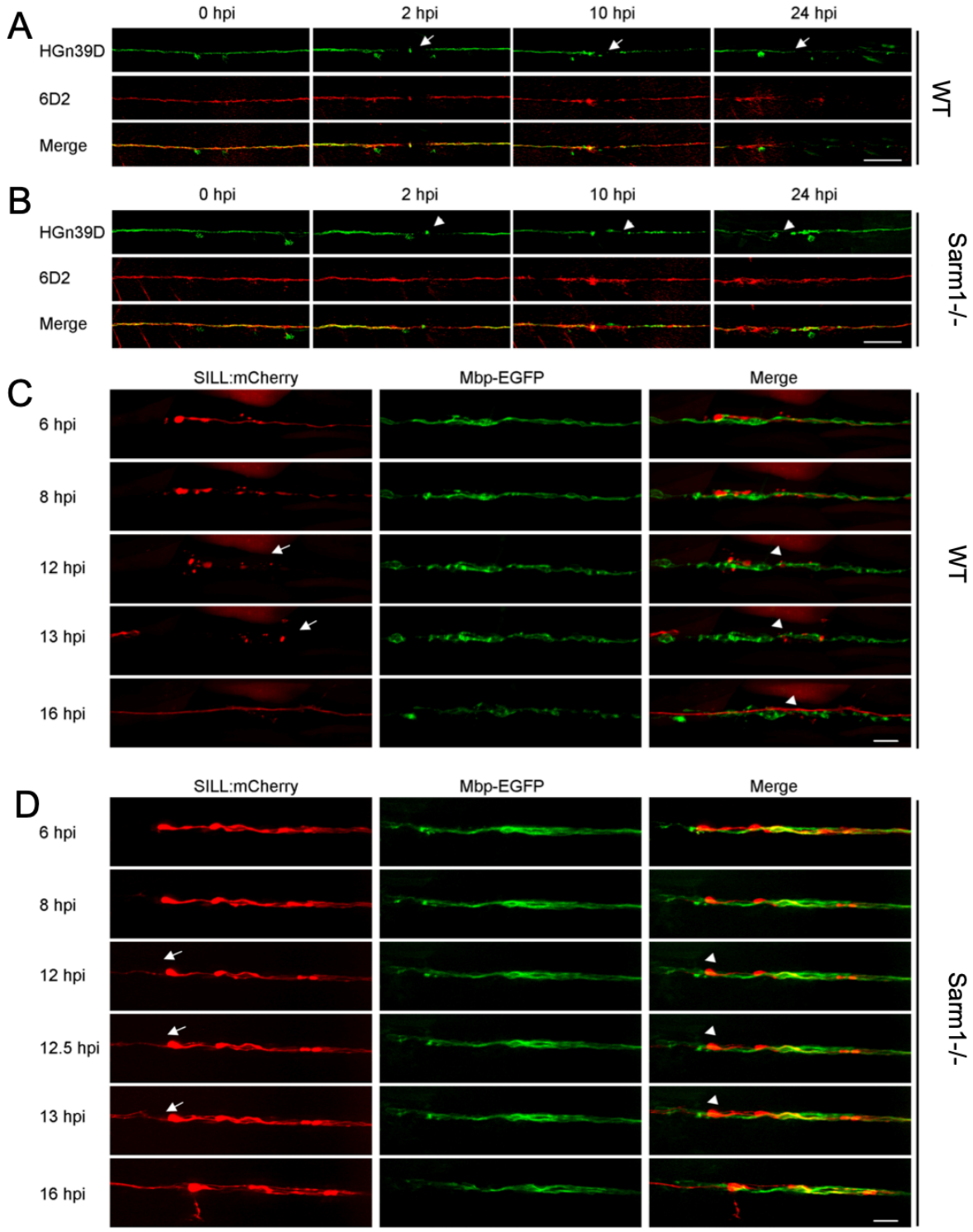


940

941 **Figure 6. A-B)** Confocal images of wild type (A) and Sarm1-/- (B) specimens
942 expressing EGFP in sensory neurons of the lateral line (green) and stained with the
943 monoclonal antibody 6D2. Stainings were performed at indicated time points after

axons severing (hpi). The arrows point to the cutting sites. Scale bar is 50μm. **C)** Live imaging of the *Tg[Mbp-EGFP; SILL:mCherry]* after severing. The arrows indicated the fragmented axons and the arrowheads the fragmented myelin. Scale bar 20μm. **D)** Live imaging of the Sarm1-/- in *Tg[Mbp-EGFP; SILL:mCherry]* after severing. Arrows indicate regrowing axons, and arrowheads indicate the juxtaposition between the regrowing axons. Scale bar 20μm.

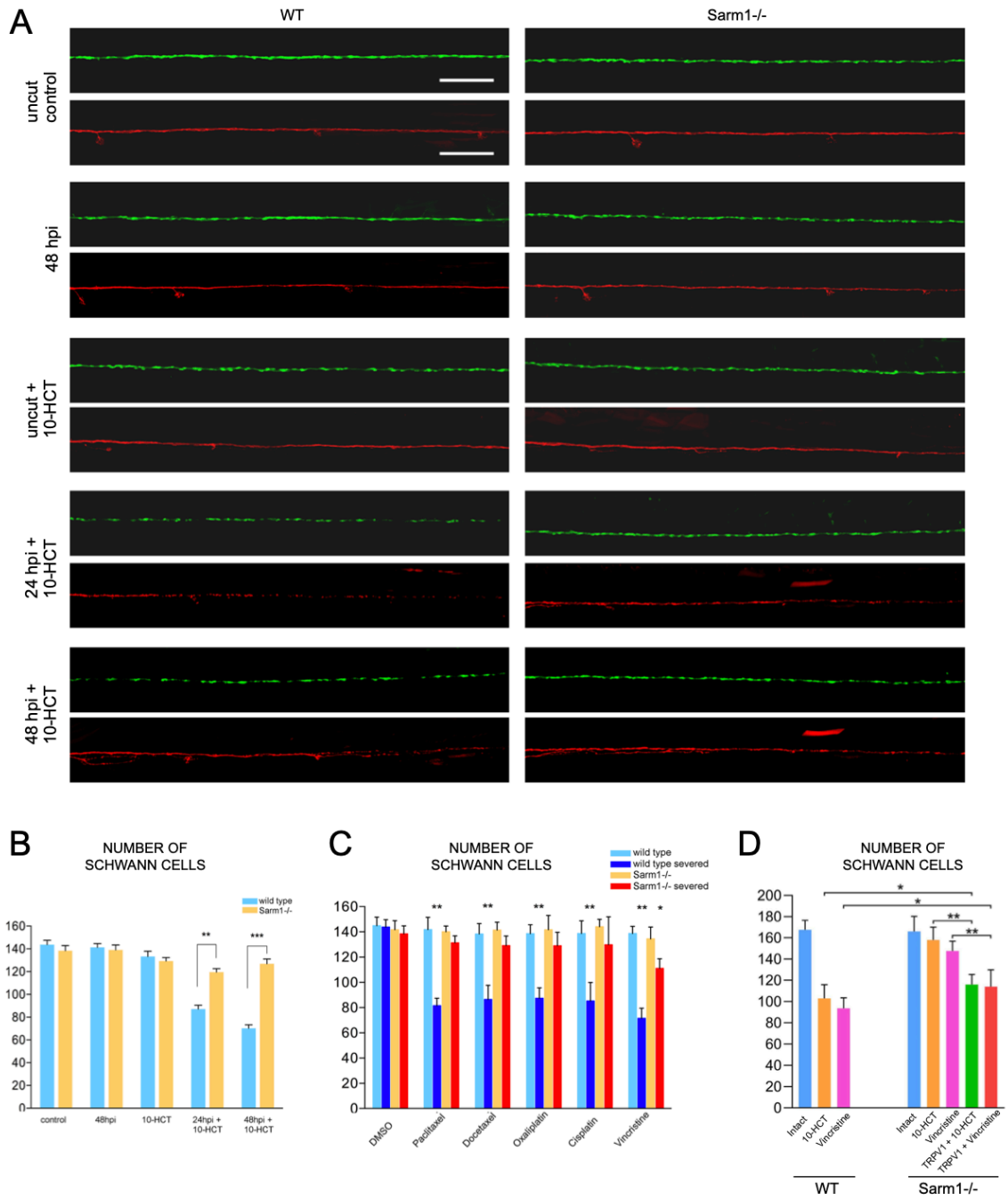


**Figure 7. A)** Confocal images showing Schwann cells (green) and lateralis sensory axons (red) in a control specimen (in which axons were not transected), in a specimen 48 hours after axon transection, and in specimens treated with 10-HCT (10-Hydroxycamptothecin). Left column is wild type and right column shows Sarm1-/-. In all cases, the concentration of 10-HCT in water was 40µm. Scale bar 100µm. **B)** Quantification of the Schwann cells from A). Data are shown as mean ± SEM. ** means $p < 0.01$, one-way ANOVA, $n = 8$ (each group). **C)** Quantification of

959 Schwann cells of WT, WT severed, Sarm1-/- and Sarm1-/- severed with the
960 treatment of the indicated chemical compounds for 48 hours. Concentrations:
961 Paclitaxel 40μm, Docetaxel 0.1μm, Oxaliplatin 500μm, Cisplatin 50μm, Vincristine
962 50μm. Data are shown as mean ± SEM. * means $p < 0.05$; ** means $p < 0.01$, one-
963 way ANOVA, n = 8 (each group). **D)** Quantification of Schwann cells after axon
964 severing, in specimens treated with 10-HCT or Vincristine. Left bar group is wild
965 type. Right bar group is Sarm1-/-, and Sarm1-/- with synthetically-eliminated axon
966 segments.
967
968
969
970
971
972 **SUPPLEMENTAL MATERIALS**

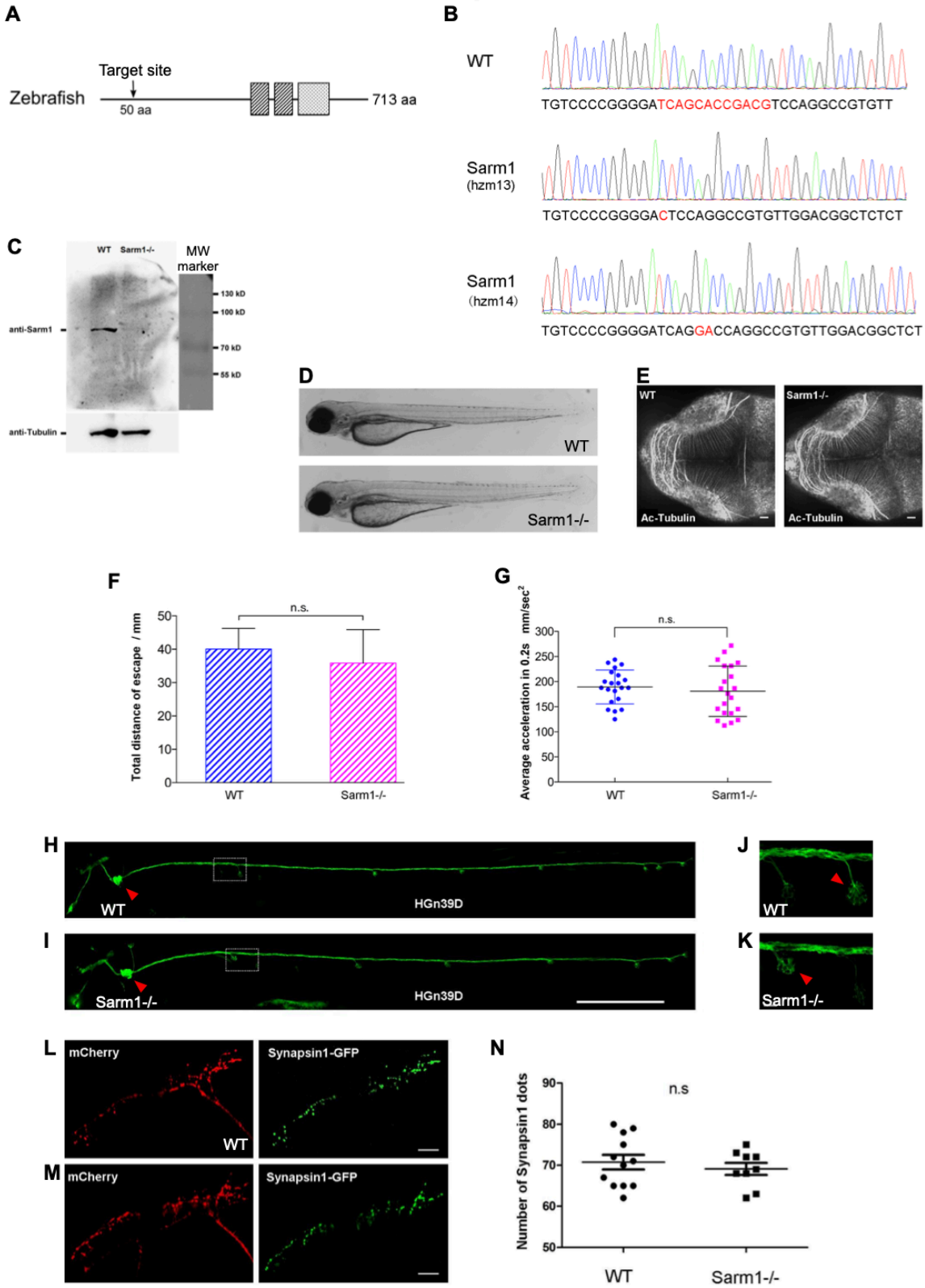


**Supplemental Figure 1. A)** Structure of the zebrafish Sarm1 protein highlighting the two SAM domains (dark grey), the TIR domain (light grey). The downward arrow indicated the approximate region targeted for mutagenesis, approximately 50

977 amino acids from the start codon. **B)** Sequence of the wild-type Sarm1 indicating in
978 red the mutagenized area and, below, the two mutant alleles obtained in this study.
979 The *hzm13* allele introduces an 11-base deletion and T/C mutation, resulting in a
980 frame shift and premature stop codon. The *hzm14* allele is a 7-base deletion and
981 AG/GA mutation that also generates a frame shift and premature stop codon. **C)**
982 Western blot of protein extracts from wild type and Sarm1$^{hzm13}$ fish embryos using a
983 commercial ant-Sarm1 antibody, revealing absence of the protein in the mutants. An
984 antibody to alpha-Tubulin was used as loading control. **D)** Low-magnification image
985 of a wild-type 5dpf zebrafish (top) and a homozygous Sarm1$^{hzm13}$ (bottom), showing
986 no overall anatomical differences. **E)** Confocal image of a wild-type 5dpf zebrafish
987 (left) and a homozygous Sarm1$^{hzm13}$ (right) stained with an antibody to acetylated
988 Tubulin to mark neurons in the central nervous system, showing no evident defects
989 in the mutants. In this and all figures, rostral is left and caudal is right. Scale bar
990 20µm. **F-G)** Quantification of sensorimotor function in zebrafish. (H) shows the total
991 distance traveled by larvae after touch-trigger escape response in wild-type (dashed
992 blue bar) and homozygous Sarm1$^{hzm13}$ (dashed magenta bar). (I) dot plot of the
993 average acceleration of wild-type (blue) and homozygous Sarm1$^{hzm13}$ (magenta) after
994 tactile touch-induced escape response. Error bar = SEM; n.s. means no significant
995 difference, Student's t test. wild type n=21, Sarm1-/- n=21. **H-I)** Confocal image
996 of a 5dpf wild-type (H) and Sarm1-/- (I) larvae carrying the *Tg[HGn39D]* transgene
997 to mark lateralis afferent neurons with GFP. The posterior lateral-line ganglion is
998 indicated with a red arrowhead. The dotted box indicates an innervated neuromast
999 (expanded in C). Scale bar 400µm. **J-K)** Confocal image of the peripheral
1000 arborization of lateralis neurons in 5dpf wild-type (H) and Sarm1-/- (I). Red arrows
1001 indicate the position of a neuromast from the dotted boxes in (H-I). **L-M)** Confocal
1002 image of the central arborization of lateralis neurons in 5dpf wild-type (L) and Sarm1-
1003 /- (M), mCherry (red) and Synapsin1-GFP (green) to reveal normal arborization and
1004 pre-synaptic puncta in both cases. **N)** Quantification of the number of synapsin1
1005 puncta from (E-F), Error bar = SEM; n.s. = not significant, Student's t test. Wild type
1006 n=15, Sarm1-/- n=15.

1007

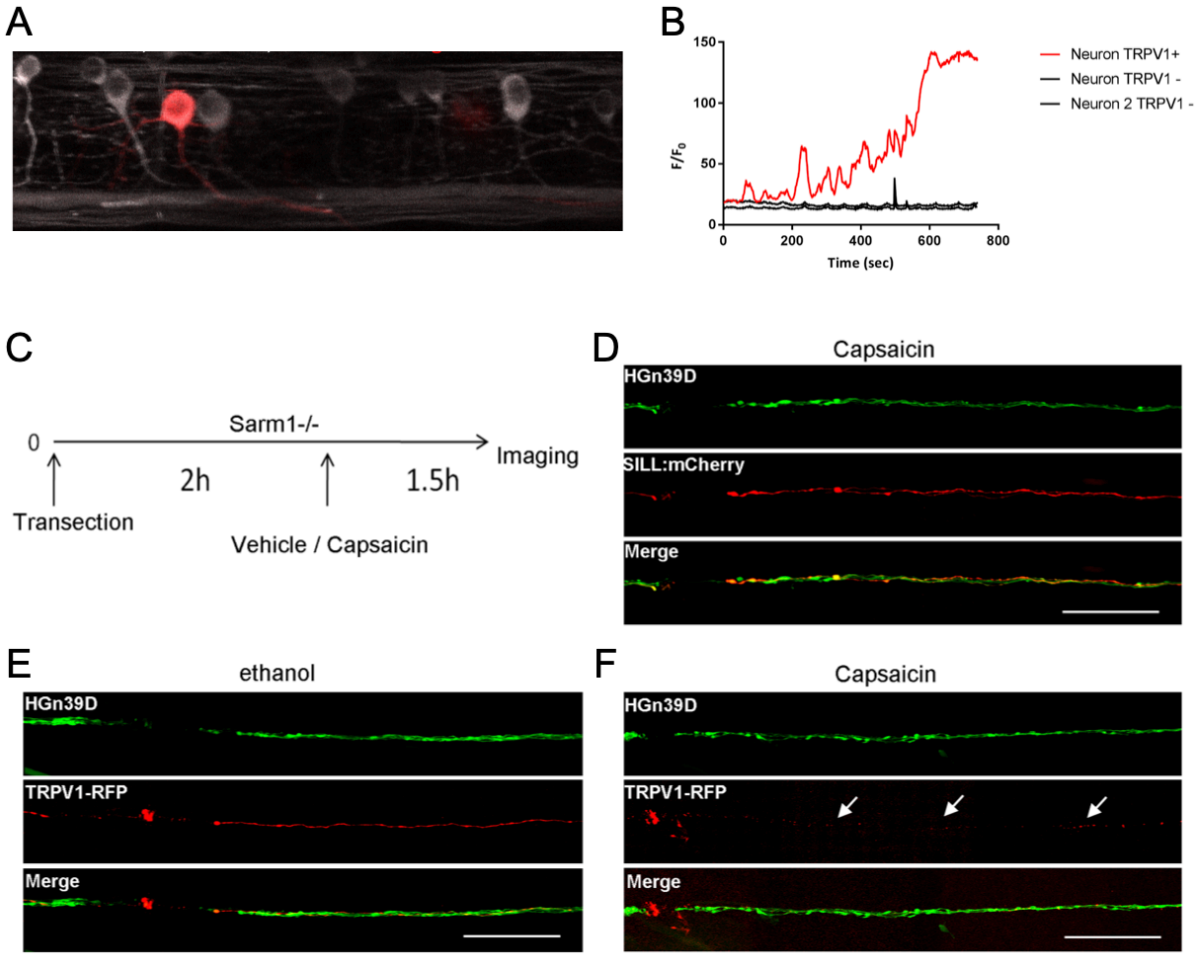


1008

1009 **Supplemental Figure 2. A)** Confocal image of UAS-TRPV1-tagRFP1 (red,
1010 injected) and UAS-GCaMP (green, transgenic) labeled neurons with
1011 Cntn1b:KalTA4. **B)** Quantification of the calcium signal after capsaicin incubation.
1012 Red plot indicated the TRPV1 positive neuron. The black plots indicated two
1013 TRPV1 negative neurons. **C)** Schematic representation of the experimental strategy
1014 to synthetically elevate calcium in Sarm1-deficient transected axons. Lateralis
1015 sensory neurons were made to express a transgene coding for the rat transient
1016 receptor potential cation channel subfamily V member 1 (TRPV1) fused to RFP, or
1017 simply mCherry. Two hours after axon transection, zebrafish larvae were bathed in
1018 ethanol solution (control), or ethanol containing capsaicin, a natural activator of
1019 TRPV1. 90 minutes after treatments, larvae were imaged by confocal microscopy to
1020 assess the extent of distal segment degradation. **D)** Sarm1-/- fish expressing GFP in
1021 all lateralis neurons (*Tg[HGn39D]*) and mCherry in a mosaic manner in some neurons.

1022 Scale bars 100μm. **E)** Sarm1-mutant fish expressing GFP in all lateralis neurons and
1023 TRPV1-RFP in a mosaic manner. Scale bars 100μm. **F)** Sarm1-mutant fish
1024 expressing GFP in all lateralis neurons and TRPV1-RFP in a mosaic manner.
1025 Capsaicin treatment induced transected axon degradation (former location of the
1026 axon signaled by three white arrows). Scale bars 100μm.
1027

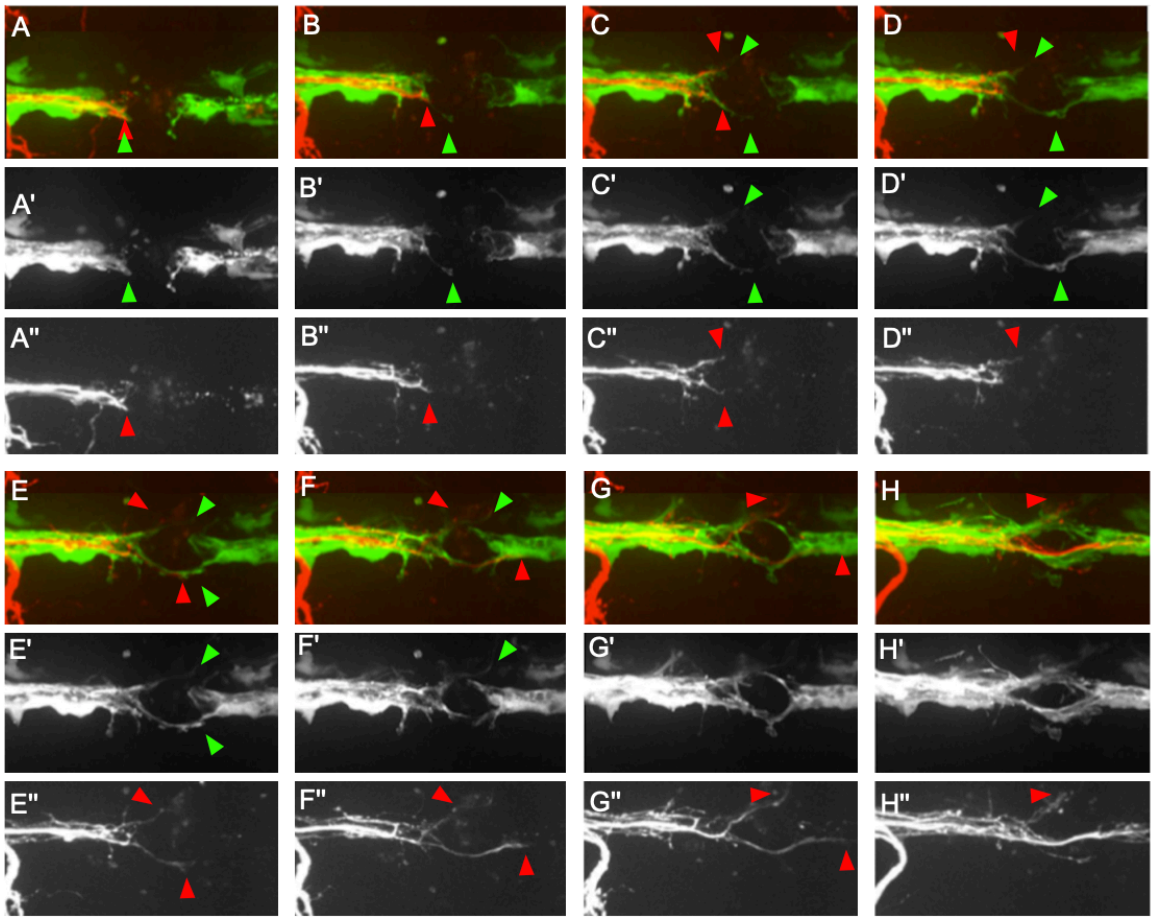


1028
1029 **Supplemental Figure 3.** Series of still images taken from Supplemental Movie 1
1030 (also shown in Figure 6, panel E). They show eight time points during the repair of
1031 the gap in the glial scaffold (A'-H') and axonal regeneration after transection (A''-H'')
1032 in a wild-type animal. Rostral is left and caudal is right. In all panels, the red
1033 arrowheads signal the location of the pioneering growth cone of the regenerating
1034 axons. The green arrowheads mark the filopodia-like extensions from Schwann cells
1035 adjacent to the glial gap. At the start of the series, the axonal terminal stump and the
1036 Schwann cells proximal to the gap co-localize (juxtaposition of the green and red

arrowhead). In C', a Schwann cell extends a filopodium across the gap, whereas the axons (C'') do not grow along this extension of across the gap. In D', several extensions from Schwann cells are clearly visible at the top and bottom aspects of the image. The shape of the lower extension from a Schwann cell did not change shape, suggesting that they are stabilized, perhaps through interactions with the substrate. Proximal axons (D'') start to grow along these Schwann-cell protrusions. In E', the extensions from the anterior and posterior Schwann cells have crossed the gap, physically interact and commence to reconstitute a continuous glial scaffold. The axonal projections (E''), however, have suffered a retraction towards the proximal stump. F'-H' show a continuation of Schwann cells behavior, increasing the contacts and closing the gap, which is obvious by the smaller area of the gap (distance between proximal and distal Schwann cells). F''-H'' show a more robust and persistent extension of the axonal growth cones, which grow nearly strictly along the Schwann cells extensions. Although the gap in the glial scaffold is much reduced, nerve fibers show discrete defasciculation (H'').

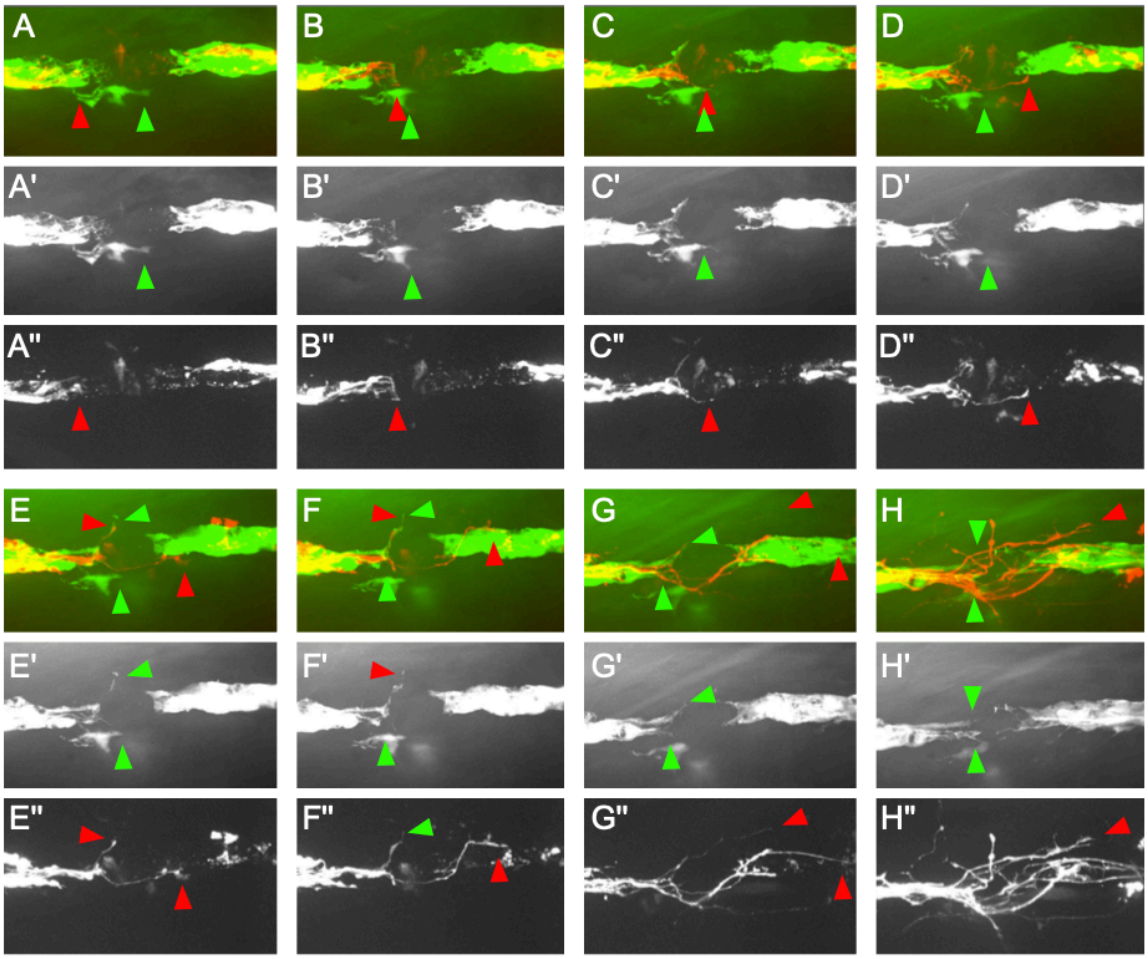


1053

1054 **Supplemental Figure 4.** Series of still images taken from Supplemental Movie 2
1055 (also shown in Figure 6, panel F). They show eight time points during the repair of
1056 the gap in the Schwann-cell scaffold (A'-H') and axonal regeneration after transection
1057 (A''-H''), in a Sarm1-mutant specimen. In all panels, the red arrowheads signal the
1058 location of the pioneering growth cone of the regenerating axons, and the green
1059 arrowheads mark filopodia-like extensions from Schwann cells. Unlike the wild-type
1060 situation shown in Supplemental Figure 1, the Schwann cells adjacent to the gap
1061 form small filopodia-like extensions, but which never cross the gap. The proximal
1062 axon stumps eventually form growth cones that cross the gap at various locations and,
1063 upon finding distal Schwann cells, grow along the glial scaffold (E''-H''). Nerve fibers
1064 show extensive local defasciculation (H'').

1065

1066 **Supplemental Movie 1.** Videomicroscopic imaging of a double transgenic
1067 *Tg[SILL:mCherry; Mfap4-memEGFP]* 4dpf wild-type specimen in which the
1068 mCherry(+) axons were severed by a laser pulse. The video represents for 13 hours
1069 of continuous imaging at a 5-minute temporal resolution. Axons (red) and
1070 macrophages (green) were visualized relative to the cut (proximal is on the left and
1071 distal in on the right).
1072
1073 **Supplemental Movie 2.** Videomicroscopic imaging of a double transgenic
1074 *Tg[SILL:mCherry; Mfap4-memEGFP]* 4dpf specimen that was mutant for Sarm1, in
1075 which the mCherry(+) axons were severed by a laser pulse. The video represents for
1076 13 hours of continuous imaging at a 5-minute temporal resolution. Axons (red) and
1077 macrophages (green) were visualized relative to the cut (proximal is on the left and
1078 distal in on the right).
1079
1080 **Supplemental Movie 3.** Videomicroscopic imaging of a double transgenic
1081 *Tg[SILL:mCherry; Mfap4-memEGFP]* 4dpf specimen that was mutant for Erbb2, in
1082 which the mCherry(+) axons were severed by a laser pulse. The video represents for
1083 13 hours of continuous imaging at a 5-minute temporal resolution. Axons (red) and
1084 macrophages (green) were visualized relative to the cut (proximal is on the left and
1085 distal in on the right).
1086
1087 **Supplemental Movie 4.** Videomicroscopic imaging of a 4dpf wild-type specimen
1088 carrying three transgenes Tg[SILL:mCherry; gSAGFF202A; UAS:EGFP], showing
1089 the dynamics of axons and Schwann cells after axonal transection. Sensory axons are
1090 shown in red and Schwann cells in green. The movie is a maximal projection of
1091 confocal stacks. It was recorded during 12 hours at 10-minute intervals. The top
1092 panel shows the merged images, the middle panel the Schwann cells, while the
1093 bottom panel the axons.
1094

1095 **Supplemental Movie 5.** Identical experiment as shown in Supplemental Movie 1,
1096 but conducted in a Sarm1-mutant specimen. It was recorded during 12 hours at 10-
1097 minute intervals. The top panel shows the merged images (SILL:mCherry;
1098 gSAGFF202A; UAS:EGFP), the middle panel the Schwann cells (gSAGFF202A;
1099 UAS:EGFP), and the bottom panel the axons (SILL:mCherry).
1100
1101
1102